Research Square

Preprints are preliminary reports that have not undergone peer review.
They should not be considered conclusive, used to inform clinical practice,
or referenced by the media as validated information.

Biomechanical consequences of coronal-plane malalignment in the knee: a finite element and configurational-force analysis of compartmental stress redistribution and cartilage damage

Dolly Kaushik
Indian Institute of Technology Ropar
Rohit Upadhyaya
Indian Institute of Technology Ropar
Sudha Bind
Max Super Speciality Hospital
Atharva Poundrik
Indian Institute of Technology Ropar
Abhishek Tiwari
abhishek.tiwari@iitrpr.ac.in
Indian Institute of Technology Ropar

Research Article

Keywords: valgus and varus deformity, knee joint biomechanics, finite element analysis, articular cartilage, meniscus, configurational forces

Posted Date: June 23rd, 2026

DOI: https://doi.org/10.21203/rs.3.rs-10103343/v1

License: This work is licensed under a Creative Commons Attribution 4.0 International License.
Read Full License

Additional Declarations: No competing interests reported.

Biomechanical consequences of coronal-plane malalignment in the knee: a finite element and configurational-force analysis of compartmental stress redistribution and cartilage damage

Dolly Kaushik[†a], Rohit Upadhyaya[†b], Sudha Bind[c], Atharva Poundrik[a], Abhishek Tiwari[b,*]

[a]*Department of Biomedical Engineering, Indian Institute of Technology Ropar, Rupnagar, Punjab 140001, India*

[b]*Fracture Mechanics Lab, Department of Metallurgical and Materials Engineering, Indian Institute of Technology Ropar, Rupnagar, Punjab, 140001, India*

[c]*Department of Cardiac Anaesthesia, Max Super Speciality Hospital, Mohali, Punjab, 160055, India*

Abstract

Valgus and varus knee deformities alter the mechanical axis of the lower limb, producing a pathological redistribution of von-Mises stress (VMS) within the joint and increasing the susceptibility of specific tibiofemoral compartments to degeneration. In this work, an anatomically reconstructed finite element model of the knee is developed that combines elastic-plastic bone modelling with a ductile damage criterion, spatially varying cortical thickness, Neo-Hookean hyper-elastic cartilage, and orthotropic elastic menisci, in order to investigate the biomechanical response to valgus and varus malalignment. Models were generated for valgus ($+5°$, $+10°$, $+15°$) and varus ($-1°$ to $-15°$) configurations under body-weight loading applied along the mechanical axis. The results reveal asymmetric VMS distributions for equivalent valgus and varus magnitudes, with the femoral cartilage and meniscus identified as the constituents most susceptible to damage. Even mild varus deformities of $-1°$ to $-4°$ generated stresses that exceed the meniscal failure limit, indicating clinically significant biomechanical consequences. Motivated by the higher damage susceptibility of cartilage, the fracture behaviour of a hyper-elastic material was further examined using a three-dimensional Compact Tension (CT) specimen containing a nearby hole. A configurational-force-based J-integral analysis showed that the hole significantly influences the crack driving force and alters the

[*†]**Both of these authors are the first authors of the manuscript and have equally contributed.**

[*]Corresponding author.

Email address: abhishek.tiwari@iitrpr.ac.in ()

expected crack propagation behaviour within the hyper-elastic material.

Keywords: valgus and varus deformity, knee joint biomechanics, finite element analysis, articular cartilage, meniscus, configurational forces

1. Introduction

The knee is among the largest and most intricate load-bearing joints of the human body, playing a central role in sustaining biomechanical function and in facilitating coordinated movement. It is supported by osseous structures such as the femur, tibia, fibula and patella, together with an array of soft tissues including the cartilage, menisci, ligaments, muscles and tendons. The joint is composed of two principal articulations, the tibiofemoral and the patellofemoral joint; the former serves as the principal load-transmission interface between the femur and tibia, while the latter governs the mechanical efficiency of the extensor mechanism [1]. The knee allows motion across six degrees of freedom, comprising three translations (medial-lateral shift, anterior-posterior drawer and distraction-compression) and three rotations (flexion-extension, abduction-adduction and internal-external rotation) [2]. Any disturbance in this coordinated kinematic interaction can give rise to a range of biomechanical abnormalities, most notably the coronal angular deformities of genu valgum and genu varum [3]. The severity and nature of these deformities are typically evaluated through the deviation of the mechanical axis relative to the knee centre and through the corresponding tibiofemoral angle [4]. The mechanical axis, or Mikulicz line, passes from the centre of the femoral head to the centre of the ankle [5].

A valgus deformity, or the knock-kneed appearance, is the condition in which the knees touch while the feet remain apart, with the mechanical axis deviating laterally relative to the centre of the knee. Conversely, a varus deformity, or the bow-legged appearance, is a condition in which the feet touch while the knees remain apart, with the mechanical axis shifting medially relative to the centre of the knee [4]. A schematic comparison of valgus and varus alignment is shown in Fig. (1). The primary tool for evaluating lower-limb alignment is the anteroposterior (AP) full-length standing radiograph, acquired with the patient standing upright to support body weight and with a horizontally focused X-ray beam directed at the hip, knee and ankle [5]. The Hip-Knee-Ankle (HKA) angle, which measures 180° in a neu-

trally aligned lower limb and is determined from full-length standing radiographs, is widely recognised as the gold-standard parameter for the radiographic detection and quantification of varus and valgus malalignment [6]. To identify the osseous origin of these deformities, whether arising in the femur or the tibia, quantification of the Lateral Distal Femoral Angle (LDFA) and the Medial Proximal Tibial Angle (MPTA) is essential; under physiologically normal conditions, both of these angles fall within the range of 85°–90°[4]. Although valgus malalignment is most commonly associated with deformity of the distal femur, recent work suggests that it may also originate from the tibia, or arise as a combined deformity involving both the femur and tibia [7]. Similarly, genu varum most commonly results from deformity of the proximal tibia, although in some cases the deformity may originate from the femur, albeit less frequently [8].

Varus malalignment is strongly associated with accelerated degeneration of the articular cartilage in the medial tibiofemoral compartment, owing to increased load transmission and elevated contact pressures. It is therefore considered a major biomechanical factor contributing to the initiation and progression of knee osteoarthritis (OA) [6]. Conversely, valgus malalignment affects the lateral tibiofemoral compartment, increasing the risk of cartilage degeneration and promoting both the onset and progression of knee OA. This process is further amplified by an increased susceptibility to meniscal damage within the mechanically overloaded lateral compartment, which accelerates joint degeneration [9]. Using functional gait analysis, Rühling et al. [10] showed that the hindfoot is unable to fully compensate for coronal-plane malalignment of the knee; as a result, varus deformity leads to narrowing of the medial ankle joint space, while valgus deformity causes narrowing of the lateral ankle joint space. These findings highlight that coronal-plane malalignment produces biomechanical effects that propagate throughout the entire lower-limb kinetic chain. Furthermore, both varus and valgus malalignment have been shown to alter patellofemoral contact mechanics and disrupt contact-area distribution, identifying coronal-plane deformities as important risk factors for the development and progression of patellofemoral OA [11].

Obesity and an elevated Body Mass Index (BMI) have been identified as important risk factors for the development of genu valgum, particularly among pubertal adolescents and females. Excess body weight increases the mechanical load acting on the lower limbs, pro-

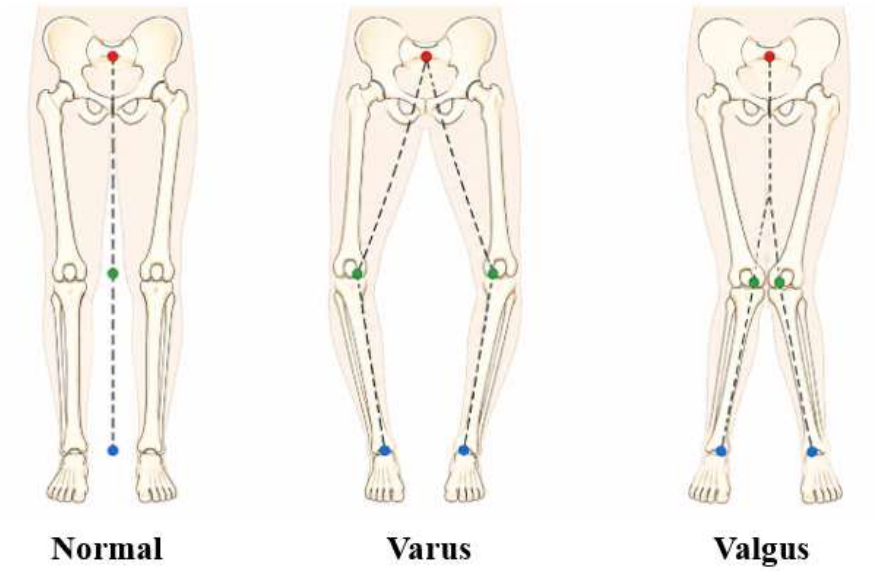


Figure 1: Comparison of normal, varus, and valgus knee alignments.

moting progressive lateral deviation of the knee over time [12, 13]. Post-traumatic valgus deformity is another recognised cause of coronal-plane malalignment and generally follows proximal tibial fractures: the increased vascularity during fracture healing can stimulate metaphyseal overgrowth, which in turn contributes to the development of valgus deformity [4]. In patients with knee OA, coronal-plane malalignment may develop as a consequence of several pathological changes, including cartilage loss, medial bone attrition, osteophyte formation, ligamentous injury, meniscal degeneration and meniscal subluxation, each of which can independently contribute to the initiation and progression of both varus and valgus deformities [14]. Vitamin D deficiency, resulting from inadequate dietary intake, insufficient sunlight exposure, or cultural practices that limit ultraviolet exposure, represents the most common nutritional cause of rickets and of its associated skeletal deformities, including coronal-plane malalignment in children. Furthermore, recent studies suggest that epigenetic mechanisms may also contribute to the pathogenesis of rickets, as alterations in DNA methylation patterns and the regulatory effects of non-coding RNAs on genes involved in bone metabolism have been proposed to influence skeletal mineralisation and, consequently, the development of bone deformities [15].

Studies examining the distribution of knee angular deformities across genders have consistently found that genu varum occurs more frequently in males, whereas genu valgum tends

to predominate in females, owing to the inherently wider pelvis and elevated quadriceps angle in females, which favour lateral-compartment loading [16]. After the age of 60 years, femoral bowing has been shown to progress towards varus in both men and women; this age-related shift is driven by a combination of reduced bone mineral density, declining muscle strength, elevated bone turnover and increasing body weight, all of which converge in the elderly to worsen coronal-plane malalignment [17]. Longitudinal measurement of the tibiofemoral angle from birth to early childhood shows that the lower limb passes through a predictable sequence of angular changes: it begins with a physiological varus that is maximal in the first year of life, reaches neutral alignment by approximately 18–24 months, then enters a phase of physiological valgus that peaks around 3–4 years of age, before gradually correcting towards the mild valgus of adult alignment by about age seven [18].

To redistribute the excessive load from the degenerated medial compartment to the comparatively healthy lateral compartment in varus deformity, High Tibial Osteotomy (HTO) is widely performed. The procedure is commonly carried out either as a medial Open Wedge (OW) or as a lateral Closing Wedge (CW) osteotomy, in which a wedge-shaped cut is created in the tibia and the corrected alignment is stabilised using plates and screws. Although both techniques provide comparable clinical outcomes, OW osteotomy generally yields slightly better functional results and a lower risk of neurovascular complications, while the two procedures differ in their effects on tibial slope and patellar height [19]. For valgus malalignment of femoral origin, Distal Femoral Osteotomy (DFO) is commonly employed to restore the mechanical axis and reduce excessive loading of the lateral compartment [20]. Several DFO techniques, including medial closing wedge, lateral opening wedge, dome and wedge-less V-osteotomy, have been described, each offering distinct advantages and limitations [21]. Owing to the limitations of cadaveric and in-vivo studies, such as specimen availability, preservation challenges and difficulties in replicating physiological loading conditions, finite element analysis (FEA) has become a reliable and cost-effective tool for evaluating stress, strain, displacement and contact mechanics in varus and valgus deformities [22].

1.1. ***Biomechanical Investigations of Valgus and Varus Deformities***

Numerous studies have used finite element analysis (FEA) to examine the biomechanical effects of varus and valgus knee malalignment. Sun et al. [23] developed three-dimensional finite element models of a healthy knee and a valgus knee from an obese child to evaluate the contact forces and von-Mises stress (VMS) distribution during gait. Their results showed a shift of peak stress and contact forces from the medial to the lateral tibial plateau in the valgus knee, highlighting the altered load transmission associated with the valgus deformity. Furthermore, greater variability in the contact-centre location was observed in the valgus model, indicating an increased susceptibility to long-term degenerative changes similar to those reported in osteoarthritic knees. The biomechanical effects of surgical correction of valgus deformity were investigated by Wu et al. [24] using computer-aided design (CAD) and FEA. Their study showed that progressive varus correction effectively reduces stress concentrations in the lateral compartment while increasing loading in the medial compartment; however, corrections exceeding 2° of varus produced an excessive increase in medial-compartment stress, indicating that alignment correction close to neutral may provide the most favourable biomechanical outcome.

Several studies have also explored the influence of varus deformity on knee joint mechanics. Ding et al. [25] showed that increasing varus alignment led to a progressive rise in the contact area and peak stress within the medial tibial cartilage, menisci and subchondral bone, accompanied by a corresponding reduction in lateral-compartment loading. These results confirmed that varus malalignment systematically shifts load-bearing towards the medial compartment and may accelerate joint degeneration. Similarly, Zhang et al. [26] showed that increasing varus angles substantially elevated medial tibial plateau stresses while reducing lateral-compartment stresses; by correlating computational results with clinical observations, the authors found that cartilage damage became significantly more prevalent when the varus angle exceeded 6°, underscoring the importance of early corrective intervention to prevent progressive osteoarthritic changes. More recent work has reinforced the sensitivity of the joint to even modest coronal deviations. Yu et al. [27] reported that the peak contact pressure in the medial compartment increased almost linearly with the varus angle, rising on average by about 0.46 MPa per degree, and that mild varus alignment el-

evated stresses within the posterior medial meniscus to a degree capable of influencing the healing potential of meniscal tears. The relevance of small alignment deviations is not limited to the native joint: in a finite element study of prosthetic malalignment, Zheng et al. [28] demonstrated that even a 2 mm medial-lateral translation of the tibial component markedly altered the proximal tibial stress distribution, again confirming that small coronal deviations can carry large mechanical consequences. Collectively, these studies show that coronal-plane malalignment profoundly alters the stress distribution and contact mechanics within the knee. Both valgus and varus deformities produce abnormal compartmental loading patterns that may accelerate cartilage degeneration and osteoarthritis progression, underscoring the value of computational modelling in understanding deformity-related joint biomechanics and in guiding corrective surgical strategies.

1.2. ***Motivation and Objective of the study***

Conventional finite element models of the knee commonly idealise bone as a purely elastic material, thereby neglecting permanent deformation and the progressive accumulation of damage under physiological loading. To overcome this limitation, the present work incorporates an elastic-plastic constitutive framework with ductile damage modelling for both cortical and trabecular bone, enabling a more realistic representation of damage initiation and failure progression. Furthermore, previous investigations have often treated bone as a homogeneous structure, overlooking the distinct mechanical characteristics of the cortical and trabecular regions as well as the spatial variation in cortical thickness. In this study, these anatomical and mechanical complexities are captured through the assignment of separate material properties and region-specific cortical-thickness distributions. In addition, a Neo-Hookean hyper-elastic constitutive model is used for the articular cartilage and an orthotropic elastic model for the meniscus, constitutive representations that have received limited attention in finite element investigations of valgus and varus malalignment. While previous studies have established that varus deformities predominantly increase loading in the medial compartment and valgus deformities in the lateral compartment, the precise sequence of damage initiation among the individual knee constituents remains insufficiently understood. This study therefore aims to investigate the influence of valgus and varus

malalignment on stress redistribution within the knee joint and to identify the constituent most susceptible to damage initiation, by comparing the predicted von-Mises stresses with the corresponding failure strengths of bone, cartilage and meniscus. Particular attention is given to examining whether equivalent valgus and varus deformities produce symmetric biomechanical responses, to determining the locations of damage initiation under moderate and severe malalignment, and to evaluating whether acute varus deformities ranging from -1° to -4° are sufficient to induce clinically significant damage. Finally, motivated by the higher susceptibility of cartilage to damage initiation, the fracture behaviour of a hyper-elastic material is investigated using a three-dimensional Compact Tension (CT) specimen containing a nearby hole, in which a configurational-force-based J-integral analysis is used to evaluate the crack driving force and the expected crack growth behaviour.

2. Material Properties

Bone is inhomogeneous across multiple length scales. Razi et al. [29] have shown that the periodic lamellae in osteons significantly influence the mechanical behaviour, as evidenced by the enhanced nominal strength and fracture energy observed in periodically inhomogeneous models. This inhomogeneous structure implies that a simplistic approach to predicting the stresses arising from malalignment in the knee joint can be highly inaccurate. The human knee joint consists chiefly of the femur and tibia, both possessing a hierarchical structure, together with the femoral and tibial cartilages, the menisci and the ligaments that constrain joint movement, each component exhibiting a distinct mechanical response. For example, bone comprises cortical and trabecular regions with different mechanical responses that are also patient-specific owing to bone mineral density, whereas the cartilage, which serves as a cushioning medium between the articulating bones, is modelled as a hyper-elastic or poro-hyper-viscoelastic material [30]. The detailed material properties used for the finite element modelling of the knee constituents are summarised in Table 1 and described below.

2.1. ***Bone***

The cortical and trabecular bone were modelled as homogeneous, isotropic, elastic-plastic materials [31] with ductile damage properties. The plastic behaviour was characterised using

yield-stress versus plastic-strain data obtained from the simulation-based work of Singh et al. [32], in which the post-yield response of each tissue was established through numerical simulation based on an ideal-plastic assumption, with the yield-strength value serving as the primary input defining the plastic response. Material failure is governed by a ductile damage criterion (independent of stress triaxiality and strain rate) incorporating a damage-evolution law, in which damage initiation was defined by the plastic strain at fracture under compressive loading, taken as 2% for cortical bone and 0.135% for trabecular bone [31]. The evolution of damage was modelled using a linear displacement-based softening law with maximum stiffness degradation, with displacement-at-failure values of 0 mm and 0.01 mm for cortical and trabecular bone respectively, beyond which element deletion may be triggered [31].

2.2. ***Cartilage***

For the femoral and tibial cartilages, a hyper-elastic Neo-Hookean formulation was adopted, with stresses governed by the following relation described by Orozco et al. [30].

$$\sigma_{tot} = \frac{1}{2}K_m\left(J - \frac{1}{J}\right)I + \frac{G_m}{J}\left(F \cdot F^t - J^{\frac{2}{3}}I\right) \tag{1}$$

where J is the determinant of the deformation gradient tensor F, I is the unit tensor, and K_m and G_m are the bulk and shear moduli defined as

$$G_m = \frac{E_m}{2(1+\nu)} \tag{2}$$

$$K_m = \frac{E_m}{3(1+2\nu)} \tag{3}$$

where E_m and ν are the Young's modulus and Poisson's ratio. This formulation represents large reversible deformation, shows the strongest correlation with the experimental crack-propagation measurements of Orozco et al. [30] across multiple loading cycles, and offers computational efficiency together with practical advantages, requiring neither fibre-orientation specification nor an extensive set of material parameters. The cartilage was assigned a density of 1050 kg/m^3 (1.05×10^{-9} Tonne/mm^3), obtained by averaging the two

independently reported values of 1000 kg/m^3 [33] and 1100 kg/m^3 [34], which falls within the accepted range for soft tissue.

Table 1: Material properties of cortical and trabecular bone, cartilage and meniscus.

Material Parameter	**Cortical Bone**	**Trabecular Bone**	**Cartilage**	**Meniscus**
ρ (Tonne/mm^3) Density	1.9e-9	1e-9	1.05e-9	1.2e-9
E_m (MPa) Young's modulus	18000	700	5	-
E_{11} (MPa) Radial elastic modulus	-	-	-	6.2
E_{22} (MPa) Axial elastic modulus	-	-	-	6.2
ν Poisson's ratio	0.35	0.35	0.174	-
ν_{12} Poisson's ratio (radial-axial)	-	-	-	0.917261
ν_{13} Poisson's ratio (radial-circumferential)	-	-	-	0.0247325
ν_{23} Poisson's ratio (axial-circumferential)	-	-	-	0.0306446
σ_u (MPa) Ultimate Tensile strength	147	2.17	-	-
Ductile Damage properties 1. ε_m^c (%) Fracture plastic strain compression 2. d_f (mm) Damage evolution	 2 0	 0.135 0.01	 - -	 - -
G_{12} (MPa) Shear modulus (radial-axial)	-	-	-	1.41
G_{13} (MPa) Shear modulus (radial-circumferential)	-	-	-	2.6
G_{23} (MPa) Shear modulus (axial-circumferential)	-	-	-	2.6

2.3. ***Meniscus***

For the menisci, an orthotropic elastic (OTE) model was employed, which more effectively captures the collagen-fibre architecture as described by Simkheada et al. [35]. This approach is comparatively simple to implement, since it excludes fluid degrees of freedom, while yielding contact areas, contact pressures, maximum principal stresses and reaction forces comparable to those of more complex models such as the Fibril-Reinforced Poroelastic

(FRPE) formulation. A cylindrical coordinate system was defined separately for the medial and lateral menisci using three orientation axes (axial, radial and circumferential), aligned with the natural collagen-fibre trajectories that follow circumferential paths. To represent the anisotropic behaviour of the meniscus, distinct elastic moduli, Poisson's ratios and shear moduli were assigned along each direction [35]. The density of the meniscus was taken as 1.2×10^{-9} Tonne/mm^3 [36].

3. Numerical Details

This section describes the construction and meshing of the finite element knee model, encompassing malalignment configurations ranging from $+15°$ to $-15°$. The procedure used to partition the bone geometry into distinct cortical and trabecular regions is outlined, followed by a description of the applied boundary and loading conditions. Finally, VMS distributions were extracted along paths traversing from the lateral to the medial compartment across all knee constituents.

3.1. ***Knee Joint geometry***

The geometries, comprising the femur and tibia, the femoral cartilage, the medial and lateral tibial cartilages, and the medial and lateral menisci, were obtained in binary STL (Stereolithography) format from the latest MBKnee_4 package [37, 38] of multibody human knee models available on the SimTK forum (https://simtk.org/frs/?group_id=765). This dataset was developed from MRI scans of the right knee of a 29-year-old female subject (mass = 70 kg, height = 170 cm).

Mesh inspection and repair were performed using two software tools. Initially, each STL file containing the meshed geometries was imported into Blender version 4.5.3 (Blender Foundation, 2025) to eliminate surface discontinuities by removing non-manifold elements and by filling holes through the Triangulate Faces feature, as shown in Fig. (2). The repaired STL files were then imported into FreeCAD 1.0 (FreeCAD Community, 2024) to assess the mesh quality, convert the part geometry into a solid body and verify its integrity. The final geometries were subsequently exported for model generation in Abaqus CAE 2018 (Dassault Systèmes, 2018). The geometries were meshed using four-node linear tetrahedral

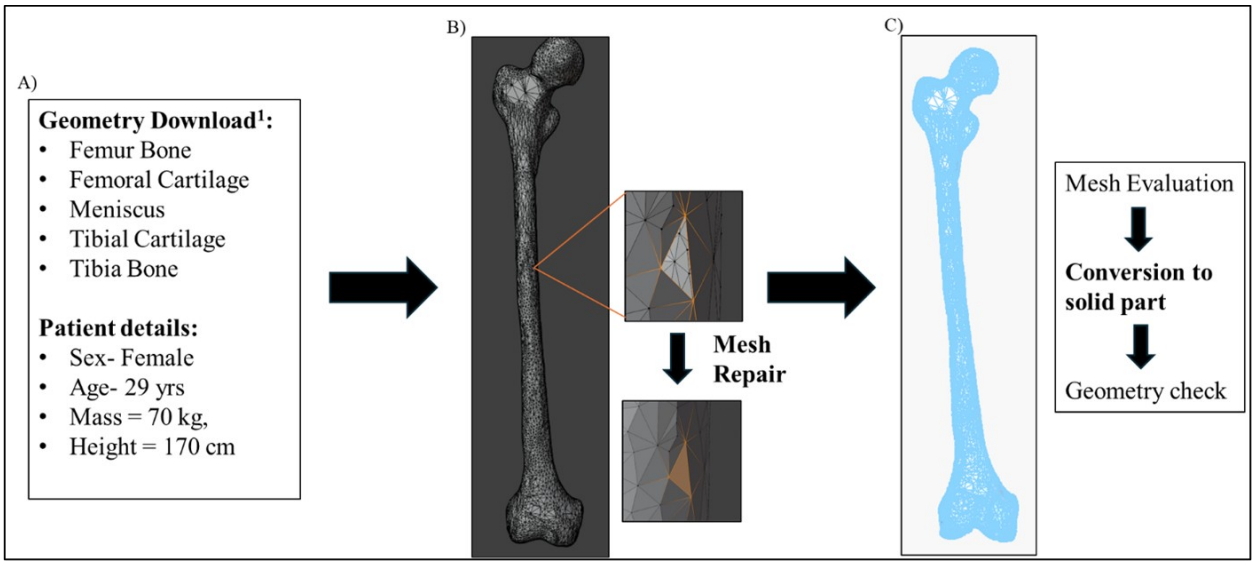


Figure 2: Geometry acquisition and conversion to a solid part. A) Geometries downloaded from the MBKnee_4 package. B) Mesh repaired in Blender (version 4.5.3). C) Geometries converted to a solid part and rechecked in FreeCAD 1.0.

elements, and the explicit solver was used for the analysis to resolve convergence difficulties. The global element size was set to approximately 3 mm for the bones, 1.5 mm for the cartilages and 1.2 mm for the menisci. This selection effectively minimised the total number of elements and, consequently, reduced both the model size and the computational load. The meshed geometries were then assembled in the same anatomical alignment and orientation as specified in the MBKnee_4 multibody model [37, 38].

3.2. ***Hip-Knee-Ankle (HKA) angle analysis***

The Femoral Head Centre (FHC) was geometrically approximated by partitioning the femoral head as a discrete region corresponding to the largest spherical bone contour, after which the volumetric centroid coordinates were extracted using the mass-properties query tool in Abaqus. This approach was adopted as an alternative to the method described by Lee et al. [39], in which the FHC is determined by identifying the centre of the circle representing the largest bone contour of the femoral head across three orthogonal imaging planes (axial, coronal and sagittal). The Knee Centre (KC) was defined as the centre of the axis joining the base of the tibial spines [40], while the Ankle Centre (AC) was established as the midpoint of the intermalleolar axis constructed by connecting the most prominent bony landmarks of the medial and lateral malleoli [41]. The three-dimensional coordinates

of these centres were then used to construct the femoral axis, extending from the FHC to the KC, and the tibial axis, extending from the KC to the AC, both serving as mathematical vectors within the model, as shown in Fig. (3). The angle between these axes defines the Hip-Knee-Ankle (HKA) angle [41], which, projected onto the coronal plane (the global x-y plane of the finite element model), was calculated to yield a varus alignment of 3.505°. To simulate the various alignment conditions, controlled rotational adjustments were applied to the femur in the coronal plane to generate valgus configurations at +5°, +10° and +15°, varus configurations at −1°, −2°, −3°, −4°, −5°, −10° and −15°, and a neutral alignment at 0°, while maintaining the tibial geometry constant across all simulations.

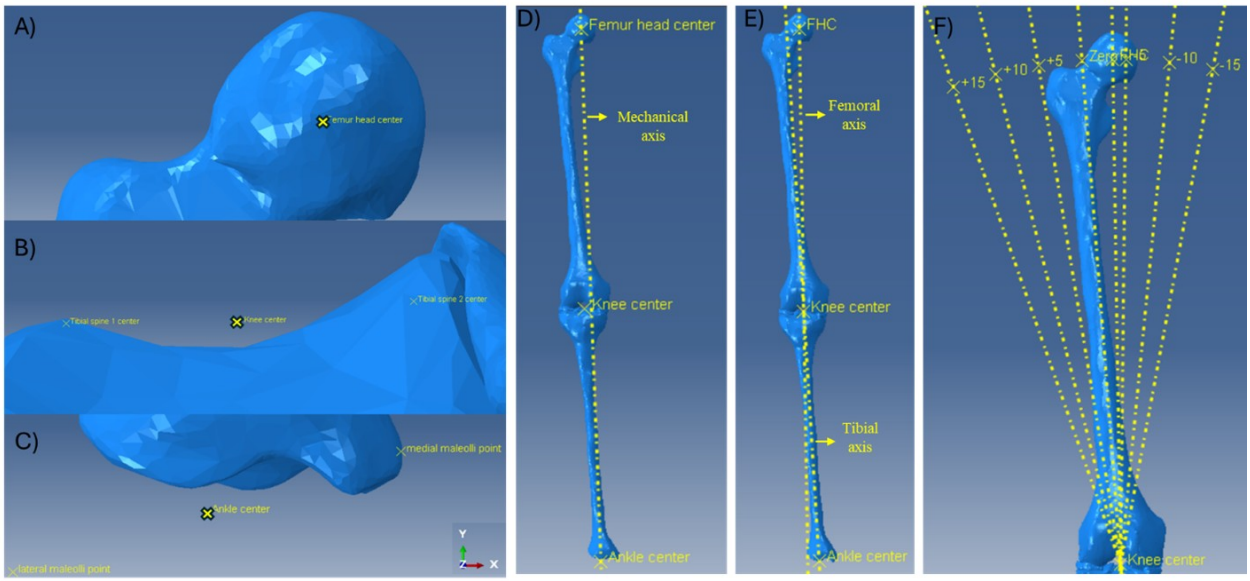


Figure 3: Hip-Knee-Ankle (HKA) analysis. A) Femoral Head Centre (FHC). B) Knee Centre (KC). C) Ankle Centre (AC), shown by a yellow cross. D) Mechanical axis. E) Femoral and tibial axes. F) Femur rotated to form valgus (+5°, +10°, +15°), neutral (0°) and varus (−5°, −10°, −15°) malalignment models.

3.3. ***Cortical and Trabecular sections***

Only the distal epiphysis of the femur and the proximal epiphysis of the tibia, with approximate lengths of 60 mm and 38 mm respectively along the proximal-distal (global y) axis, were retained for constructing the knee models; the remaining portions were excluded. These segments were subdivided into multiple parts resembling stacked cylinders, each 5 mm in height, while the segment adjacent to the cartilage was further refined into 1 mm sections, owing to its irregular surface geometry, using the Create Cut: Extrude feature. The proce-

dure used to partition the bone geometry into cortical and trabecular regions is illustrated in Fig. (4).

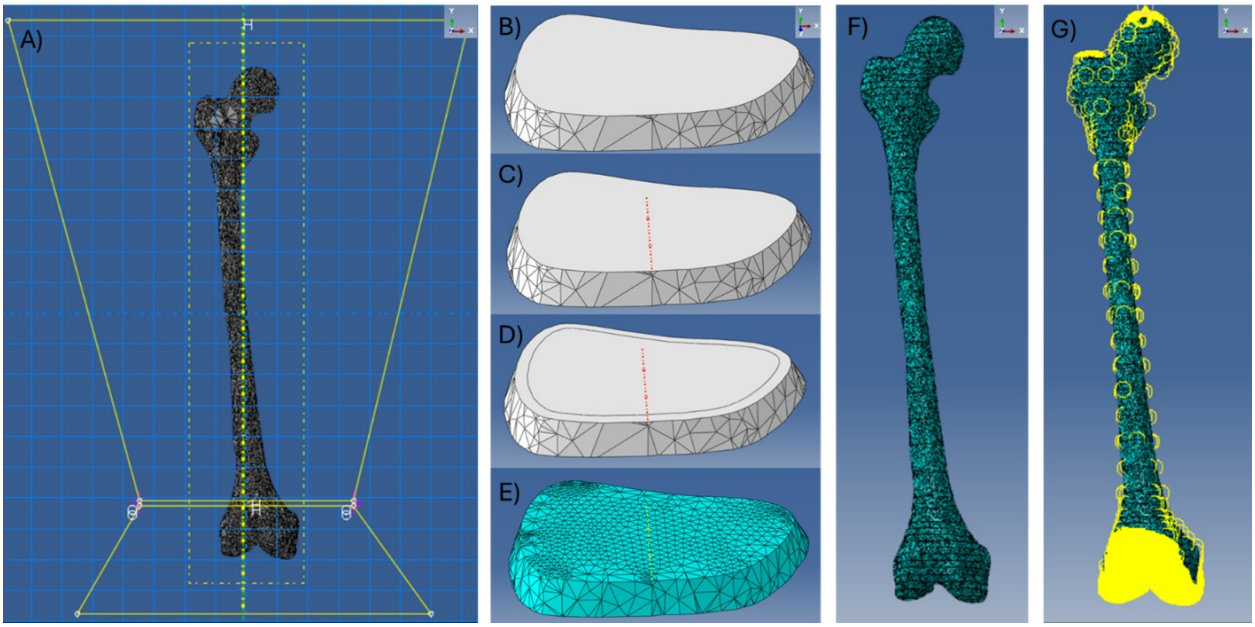


Figure 4: Partitioning of the femur into cortical and trabecular sections. A) Selection of partition coordinates for the cut created using the extrude feature. B) Individual bone part. C) Datum points and axis. D) Cortical (outer) and trabecular (inner) sections. E) Mesh. F) Assembled bone. G) Tie constraints between adjacent bone parts.

Each part was divided into an outer cortical and an inner trabecular region through the following systematic procedure. First, for each part the centroids of the upper and lower surfaces were determined by selecting their respective geometries and obtaining their mass properties. Second, these coordinates were used to generate datum points, which were subsequently connected to define a datum axis. Third, using the Create Partition: Cell feature, the outer edges of the top surface were selected through the Sketch Planar Partition tool and offset inward by 2 mm, following Brănescu et al. [42], thereby establishing the cortical-trabecular interface. Finally, using the Extrude/Sweep Edge function within the partition-cell feature, the selected interface edges were extended along the y-axis to the bottom surface, thus separating the cortical and trabecular regions into two concentric cylindrical structures.

3.4. ***Boundary conditions and Constraints***

To accurately replicate the condition of a patient standing on a single limb within the finite element analysis, the following load and boundary conditions were imposed following the methodology of Zhang et al. [26].

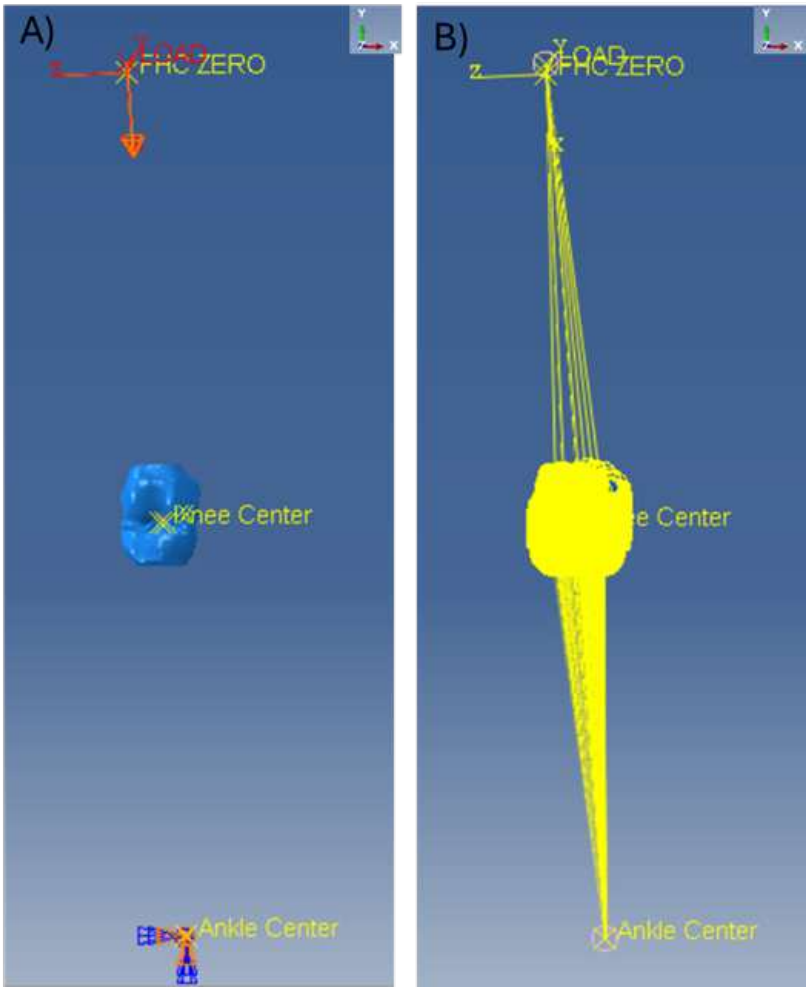


Figure 5: Load and boundary conditions. A) Load point defined along the mechanical axis above the Femoral Head Centre (FHC), with the knee model and the Ankle Centre constrained in all degrees of freedom. B) Kinematic coupling of the load point to the distal femur and of the Ankle Centre to the proximal tibia.

A local coordinate system with the FHC as origin was established, aligning the mechanical axis, defined by the line connecting the FHC and AC, with the x-axis. A load of 740 N, directed along this mechanical axis [26], was applied from a reference point positioned 10 mm above the FHC. This reference point was kinematically coupled to the top surface of the distal femoral epiphysis to ensure uniform load transfer. The femur was left unconstrained in

all degrees of freedom, while the bottom surface of the proximal tibial epiphysis was kinematically coupled to a reference point at the AC, at which all translational and rotational degrees of freedom were fully constrained [26]. The applied loading and boundary conditions are shown in Fig. (5). Contact interactions between the femoral and tibial cartilage, between the femoral cartilage and meniscus, and between the meniscus and tibial cartilage were defined as frictionless face-to-face contact with finite slip, using a hard-contact formulation to model the pressure-gap relationship [26]. Surface-to-surface tie constraints were used to establish continuity between adjacent bone parts. Similarly, the femoral and tibial cartilages were tied to their respective underlying bone surfaces [43], while the medial and lateral meniscal horns were tied to the tibial plateau [44] to maintain anatomically consistent attachment conditions throughout the model.

3.5. ***Finite element interpolation details***

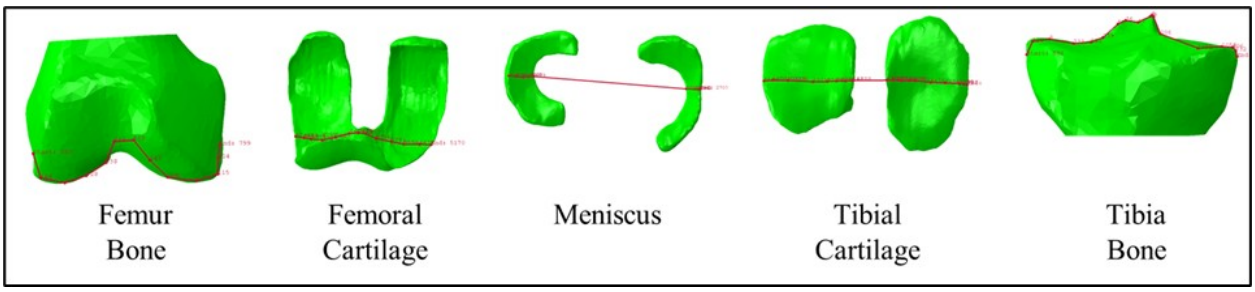


Figure 6: Paths traversing from the lateral to the medial compartment defined on the femur bone, femoral cartilage, meniscus, tibial cartilage and tibia bone.

A compressive load was increased linearly from 0 to 740 N over a simulation time of 0.001 s using dynamic explicit analysis. Semi-automatic mass scaling was applied throughout the model to ensure computational stability, with a minimum time increment of 1×10^{-9} s. Once the simulation was complete, designated paths were defined across the articular surfaces of the individual knee constituents, traversing from the lateral to the medial compartment so as to partition each component into anterior and posterior regions, with the midpoint of each path identified relative to the KC. The predefined paths used for extracting the von-Mises stress distributions across the various knee constituents are illustrated in Fig. (6). The VMS distribution was extracted along these paths to evaluate the symmetry of the mechanical response under varus and valgus alignment, specifically to determine whether

equal magnitudes of varus and valgus angulation produce comparable VMS distributions within the corresponding constituents. The VMS distribution over the entire surface of each constituent was further evaluated by analysing three-dimensional contour plots across multiple anatomical views, after which the peak VMS values were extracted and compared against the ultimate compressive and tensile strength thresholds reported in the literature, derived from experimental mechanical testing of human knee specimens.

4. Results and Discussion

To evaluate the symmetry of the VMS distribution under valgus and varus malalignment (5°, 10°, 15°), VMS-versus-distance profiles were analysed along the predefined paths for each knee constituent. The VMS analysis of the distal femur across the valgus and varus models revealed an angulation-dependent stress distribution that diverged markedly between the two malalignment types. In the valgus series, lateral condylar stresses increased progressively with angulation, reaching approximately 6 MPa at +15° compared with 2–4 MPa under the neutral condition, consistent with the lateral shift of the weight-bearing axis; concurrently, medial condylar stresses declined from 8 MPa at 0° to 6.2 MPa at +15°, reflecting systematic medial-compartment off-loading, as shown in Fig. 7 A). The varus models, shown in Fig. 7 B), exhibited considerably elevated medial condylar stresses, escalating to 10.69 MPa at −15°, approximately 72% greater than the equivalent valgus configuration, thereby confirming the well-established biomechanical predisposition to accelerated medial-compartment stresses in varus knees; the lateral-compartment stress, by contrast, was reciprocally reduced to as low as ∼3 MPa, a decrease of nearly 50%. Localised stress peaks were also observed in the −10° and −15° varus configurations around the terminal portion of the medial compartment. Notably, under both varus and valgus conditions the medial compartment sustained higher stress magnitudes than the lateral compartment, and a consistent stress concentration of ∼4–5 MPa was identified in the vicinity of the midpoint corresponding to the intercondylar region across all malalignment models.

The VMS distribution for valgus malalignment, shown in Fig. 8 A), exhibits relatively low and comparable stress magnitudes in the lateral compartment over the initial 20 mm of the path, ranging between 0.03 and 0.3 MPa; a pronounced stress escalation was then

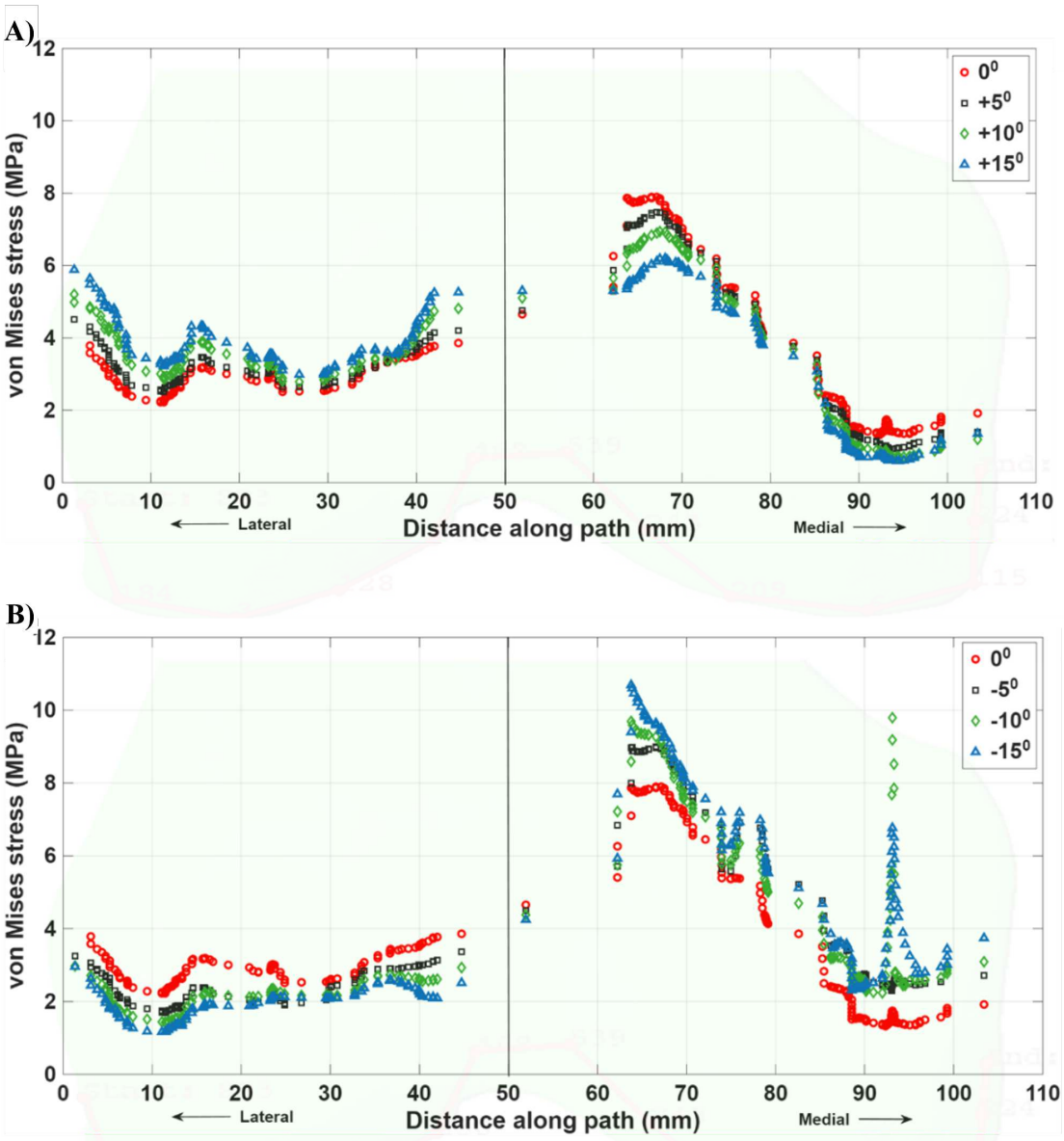


Figure 7: von-Mises stress (MPa) as a function of distance (mm) along a predefined path across the femur bone from the lateral to the medial compartment, showing an asymmetric distribution for equal magnitudes in A) valgus and B) varus models.

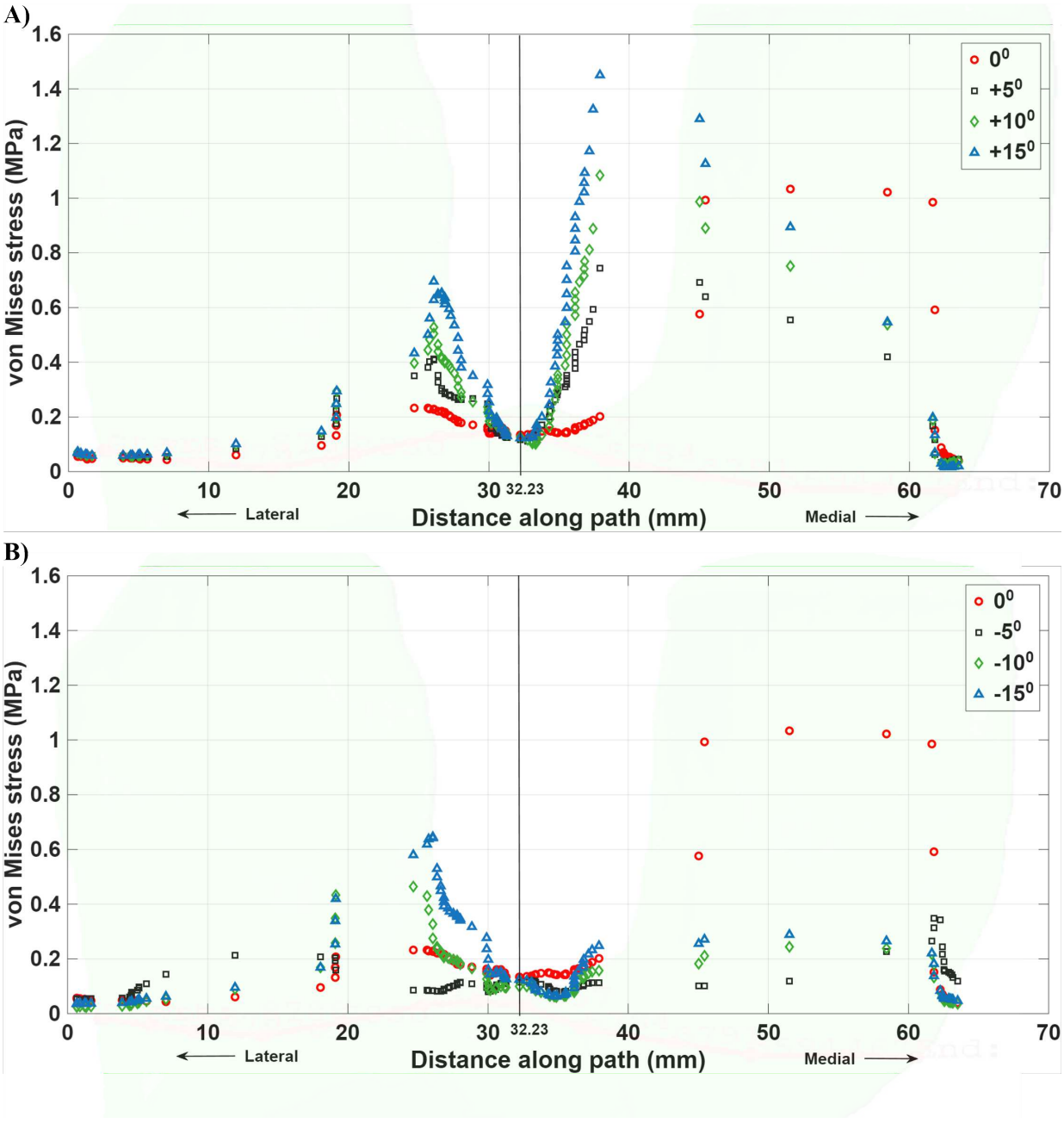


Figure 8: von-Mises stress (MPa) as a function of distance (mm) along a predefined path across the femoral cartilage from the lateral to the medial compartment, showing an asymmetric distribution for equal magnitudes in A) valgus and B) varus models.

observed for all angles between 25 and 40 mm (around the midline), where the +15° configuration attained the highest magnitude of 1.45 MPa. The medial compartment recorded higher stress concentrations despite the lateral redistribution of the weight-bearing axis. Beyond 40 mm, in the medial compartment, the stresses decreased gradually towards the terminal end, with the neutral model lying between the +15° and +10° models. The varus series, shown in Fig. 8 B), likewise exhibited higher stresses in the intercondylar zone and lateral compartment despite the medial redistribution of the weight-bearing axis. The varus configurations produced attenuated medial-compartment stresses ranging between 0.1 and 0.4 MPa, compared with about 1 MPa in the neutral alignment, rather than generating the medial stress peaks conventionally anticipated.

As shown in Fig. 9 A), with increasing angulation a marginal reduction in VMS was observed in the lateral meniscus, declining from 0.48 MPa at 0° to 0.17 MPa at +15°, while a comparatively consistent stress distribution was seen in the medial meniscus across all valgus angles. In Fig. 9 B), among the varus configurations the −5° case exhibited the most pronounced peak stress in the medial meniscus, posing a greater risk of damage than its valgus counterpart, whereas the −10° and −15° configurations yielded stress magnitudes broadly comparable to those of the neutral condition. A gradual decline was observed in the lateral meniscus with increasing varus angulation.

The tibial cartilage stress response under valgus malalignment, shown in Fig. 10 A), remains largely uniform and nearly negligible across the entire path, with a subtle stress elevation of approximately 0.15 MPa observed for all valgus angles, confined exclusively to the lateral tibial cartilage within the peri-intercondylar zone (25–32 mm). Within the same spatial zone, comparable peak VMS values were also observed for the −5° and neutral configurations, as shown in Fig. 10 B), while the −10° and −15° varus configurations exhibited nearly negligible lateral stress concentrations, indicative of lateral-cartilage off-loading with increasing varus severity. In the post-intercondylar zone, the stress magnitudes increased progressively with angulation from 0° to −15°. The −5° configuration reached the highest stress magnitude recorded across the entire tibial cartilage analysis, attaining up to 0.69 MPa within the terminal zone of the medial tibial cartilage (60–73 mm). This pronounced rise in stress indicates the critical vulnerability of the medial tibial cartilage even under modest

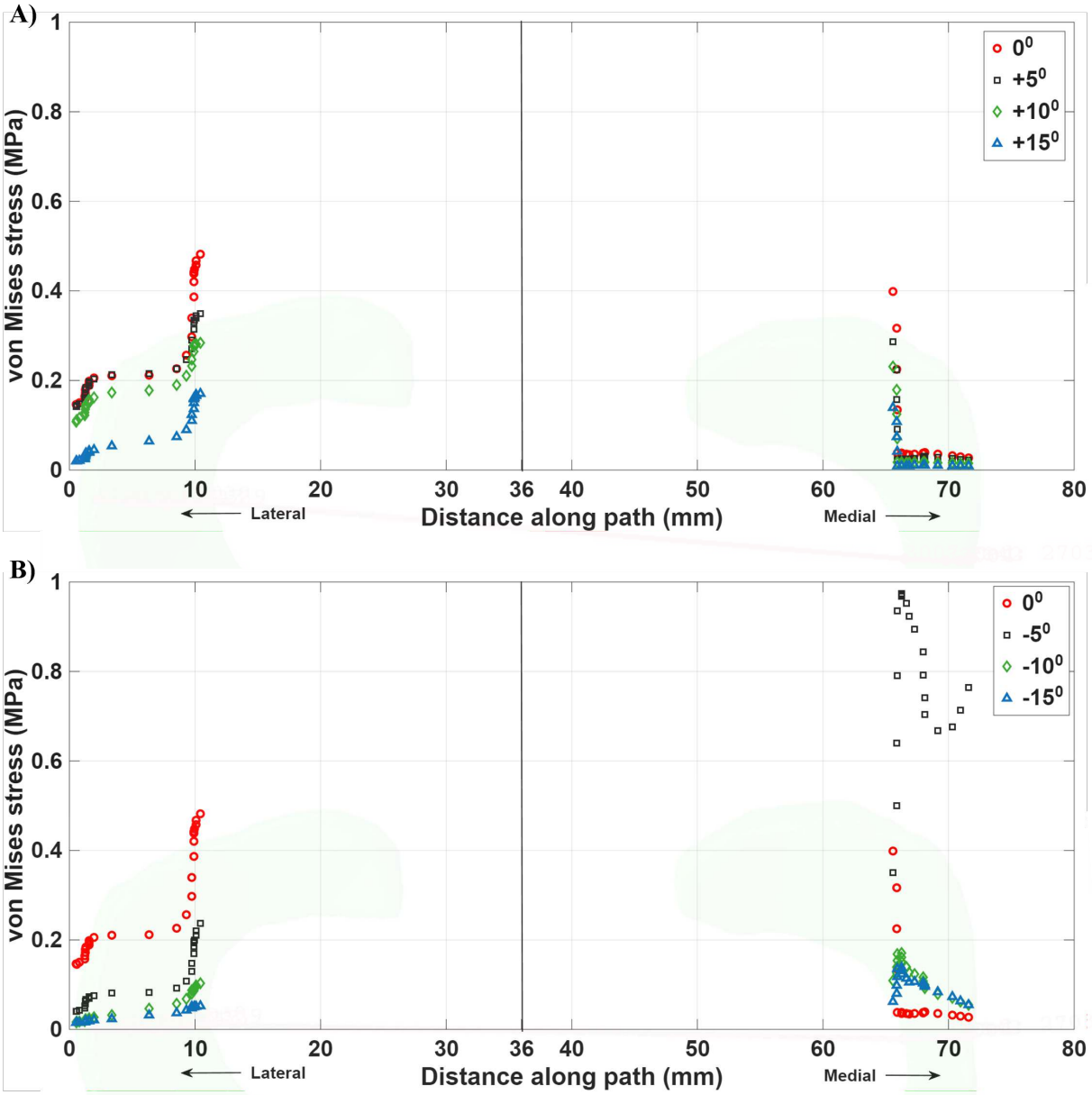
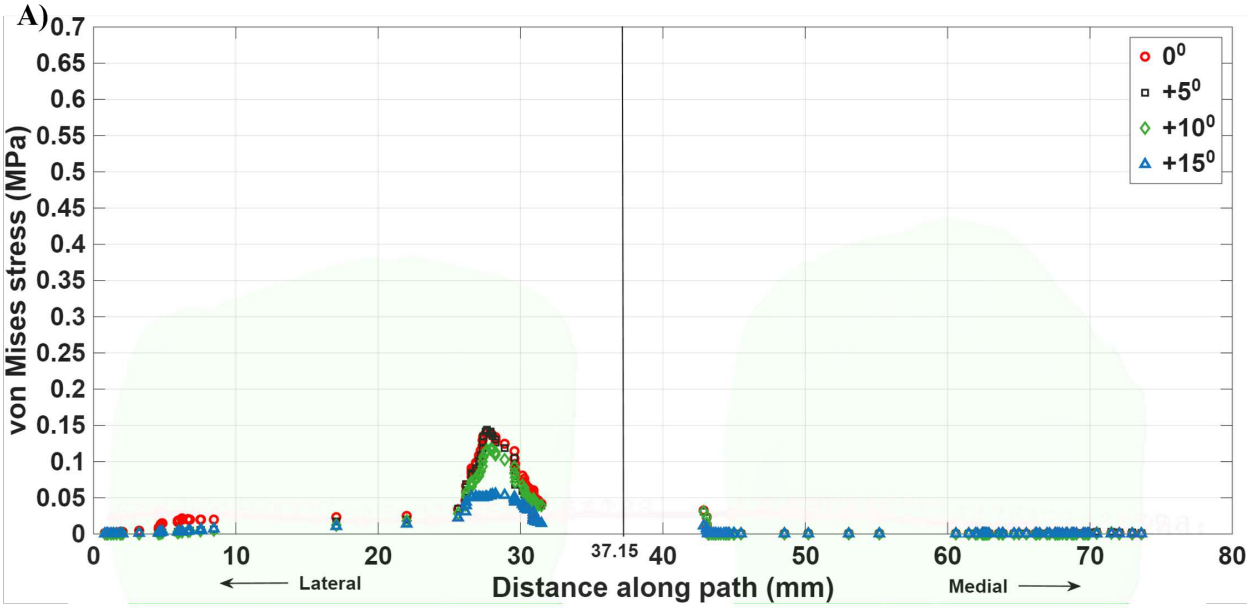


Figure 9: von-Mises stress (MPa) as a function of distance (mm) along a predefined path across the meniscus from the lateral to the medial compartment, showing an asymmetric distribution for equal magnitudes in A) valgus and B) varus models.



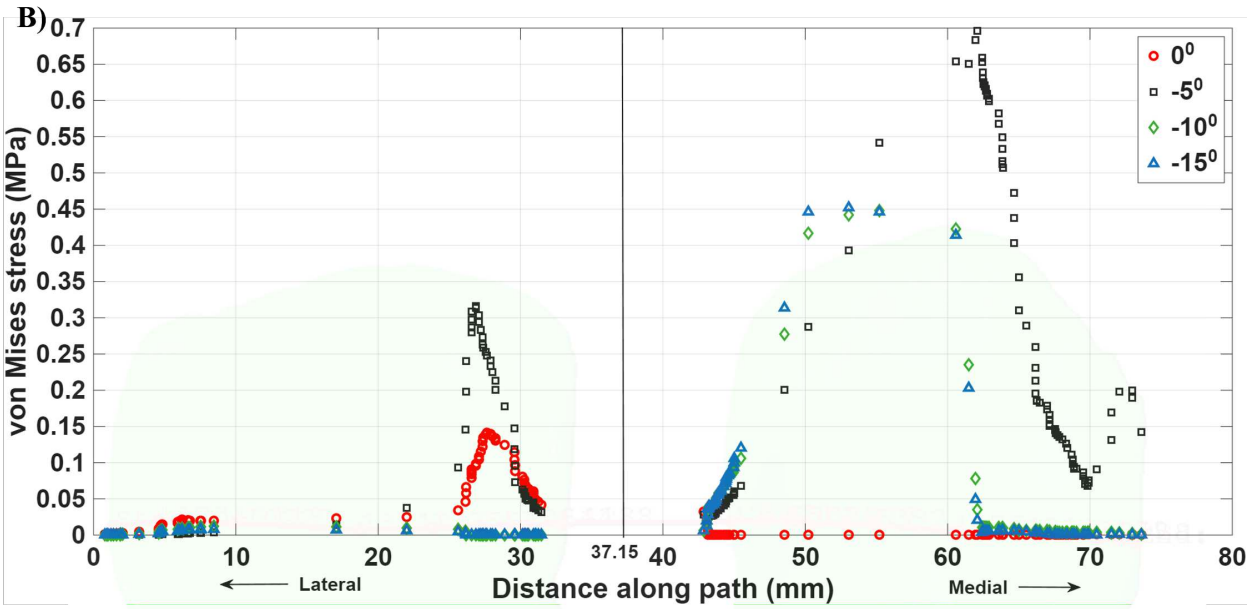


Figure 10: von-Mises stress (MPa) as a function of distance (mm) along a predefined path across the tibial cartilage from the lateral to the medial compartment, showing an asymmetric distribution for equal magnitudes in A) valgus and B) varus models.

varus malalignment.

For the tibial bone under valgus malalignment, shown in Fig. 11 A), a consistent and uniform inverse-angulation hierarchy was maintained across both the lateral and medial compartments, characterised by gently attenuating stress magnitudes throughout the designated path rather than by localised peaks in specific zones. Within the mid-lateral zone (10–40 mm), a maximum stress of approximately 0.66 MPa was observed for the neutral alignment, substantially higher than that in the overlying soft tissues (lateral meniscus and lateral tibial cartilage), indicating the greater mechanical burden borne by the tibial bone. For the varus series, shown in Fig. 11 B), the neutral and -5° configurations attained comparable peak stress concentrations of approximately 0.65–0.70 MPa in the mid-lateral zone, with the -5° configuration marginally exceeding the neutral condition; this contrasts with the valgus series, in which the neutral condition consistently dominated throughout. In the medial compartment, the -5° configuration produced the maximum VMS of approximately 1.31 MPa between 70 and 72 mm, followed by -10°, which reached the second-highest medial stress of 0.75 MPa between 56 and 57 mm, while the -15° configuration registered a moderate but still elevated medial stress of approximately 0.5 MPa relative to the most attenuated neutral condition.

To identify the sites of damage initiation among the knee constituents, the VMS distributions were systematically examined through three-dimensional contour plots generated for each constituent under the neutral condition as well as the valgus and varus configurations spanning angulation severities of 5°, 10° and 15°. The peak VMS magnitudes extracted from these contour plots were then compared with the ultimate tensile and ultimate compressive strength thresholds, listed in Table 2 and reported in the experimental literature for each component, to facilitate the identification of regions most susceptible to structural damage.

Fig. (12) shows the three-dimensional VMS contour plots of the distal femur in the posterior view, in which the right side corresponds to the lateral compartment and the left side to the medial compartment. Warm-coloured zones, indicative of elevated stress magnitudes in the range of 15–30 MPa, were concentrated along the postero-superior surface spanning both compartments, while the condylar articular surfaces retained stress magnitudes below 5 MPa, represented by the white regions in the contour. Under the neutral condition, a peak

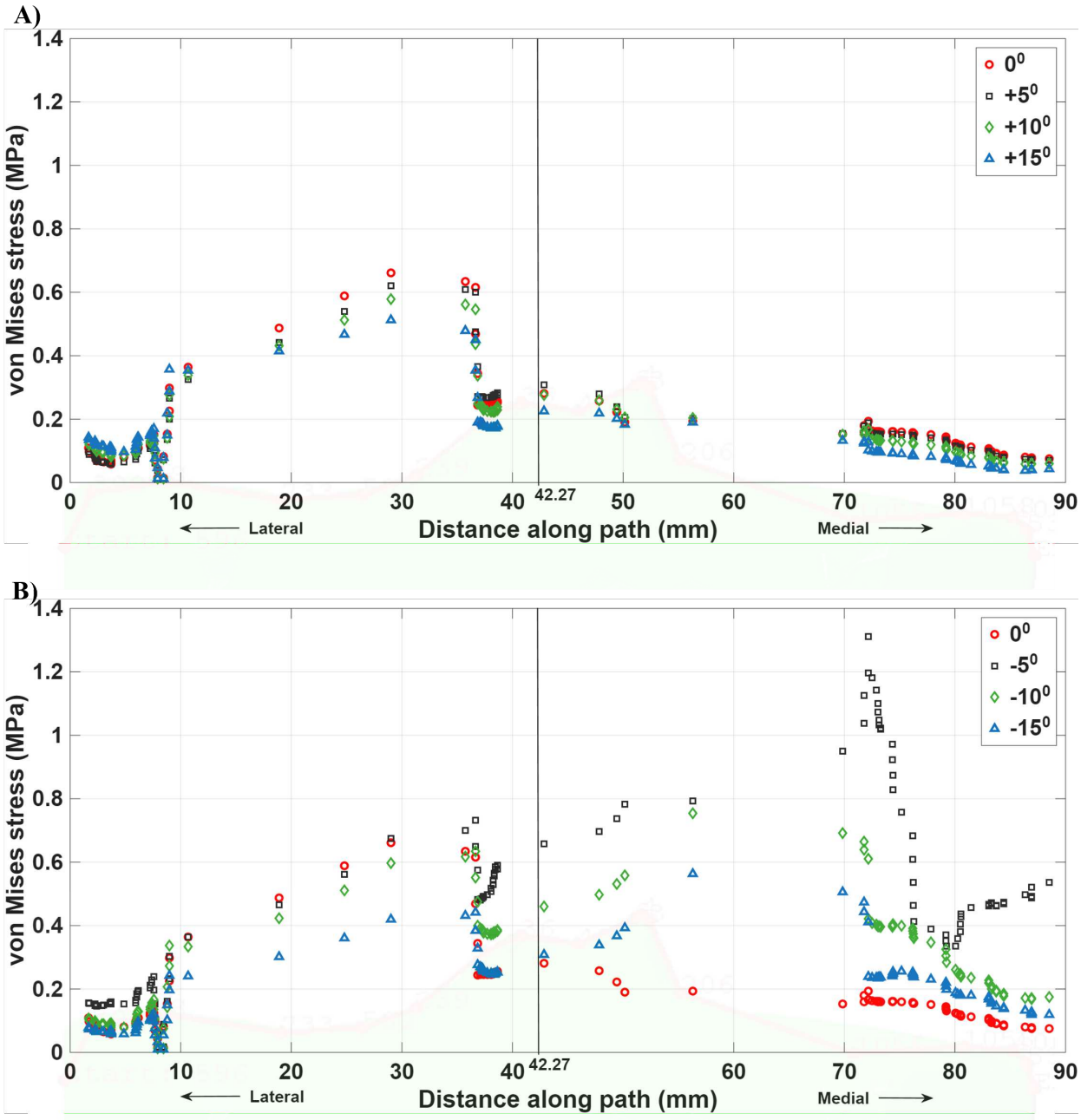


Figure 11: von-Mises stress (MPa) as a function of distance (mm) along a predefined path across the tibia bone from the lateral to the medial compartment, showing an asymmetric distribution for equal magnitudes in A) valgus and B) varus models.

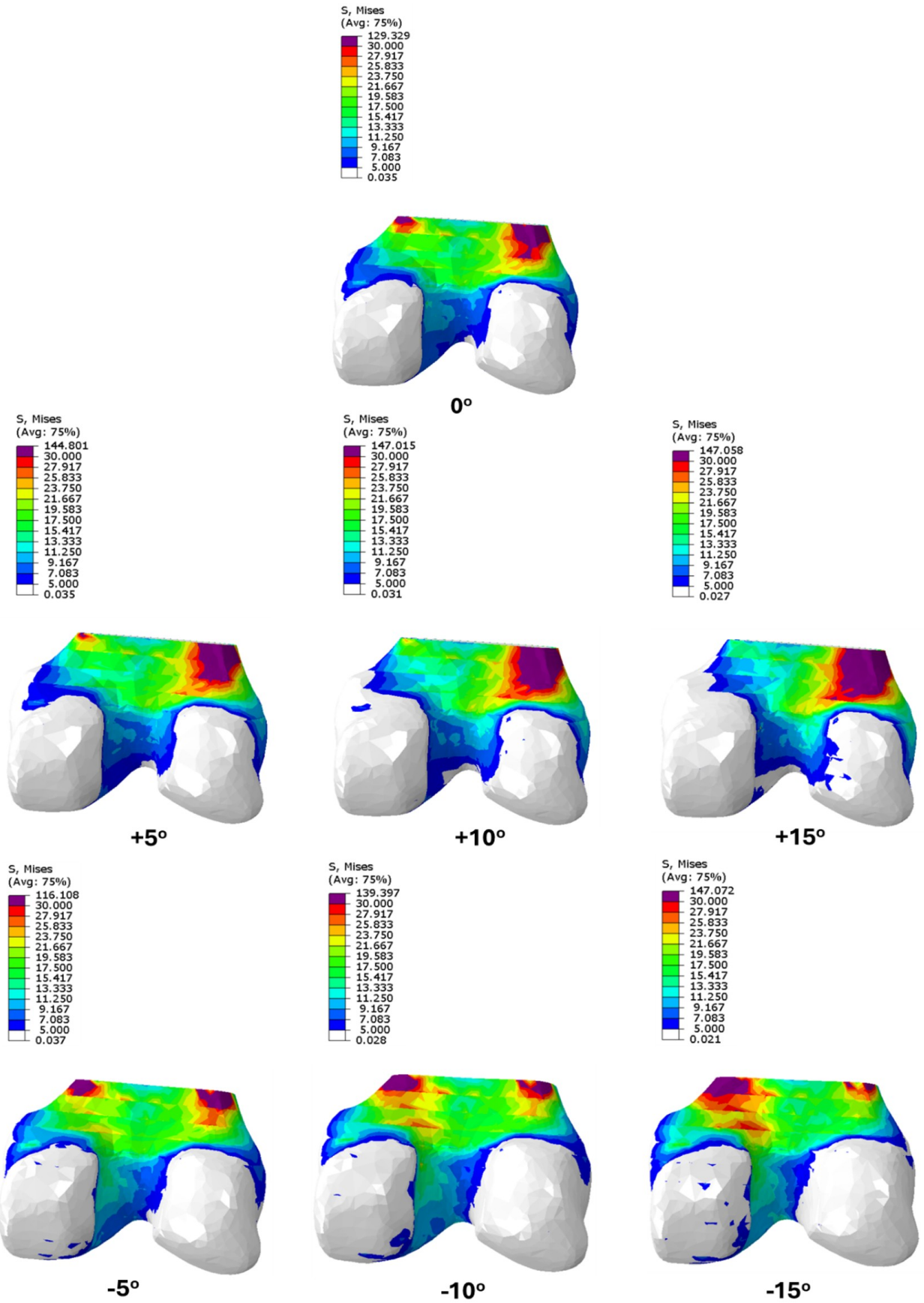


Figure 12: Three-dimensional contour plots of the von Mises stress distribution in the femur bone (posterior view), which increases on the lateral postero-superior surface in the neutral (0°) and valgus (+5°, +10°, +15°) models and on the medial postero-superior surface in the varus (−5°, −10°, −15°) models.

stress of 129.329 MPa was observed as a high-stress zone on the lateral postero-superior surface, which expanded progressively in both spatial extent and magnitude within the valgus series, escalating to 144.801 MPa at $+5°$ and reaching an approximate saturation of 147 MPa at both $+10°$ and $+15°$. In the varus series, the $-5°$ configuration exhibited a peak stress of 116.18 MPa, which increased further to 139 MPa at $-10°$ and 147 MPa at $-15°$, accompanied by a substantial expansion of the elevated stress field across the medial postero-superior surface and a reciprocal attenuation of stress in the lateral compartment. The peak VMS magnitudes recorded across all angulation conditions, including the neutral alignment, remained below the physiologically reported ultimate compressive stress of 200 MPa for cortical bone [45] and 10.16 MPa for trabecular bone [46], indicating that the stress state of the distal femur does not approach the critical failure threshold under standing loading conditions.

Across all valgus, varus and neutral configurations, the VMS distribution in the femoral cartilage, shown in Fig. (13), remained spatially localised, with discrete stress-concentration hotspots identifiable on both the lateral and medial condylar surfaces, while the predominant stress field across the bulk of the articular surface remained below 2 MPa. Examination of the three-dimensional contour plots for the valgus configurations shows a progressive escalation in the peak stress magnitude from 13.190 MPa under the neutral condition to 162.279 MPa at $+10°$, followed by a reduction to 40.763 MPa at $+15°$, with all peak concentrations localised to the lateral condylar articular surface. The recorded peak stresses substantially exceeded the ultimate strength threshold of 11 MPa reported for the lateral femoral cartilage [47], shown in Fig. 22 A), across the neutral and all valgus configurations, indicating a pronounced susceptibility to tissue failure. A similar trend was observed for the varus series, in which the maximum stress increased from 8.212 MPa at $-5°$ to 41.487 MPa at $-10°$ and then declined to 30.643 MPa at $-15°$, with all peak concentrations consistently localised to the medial condylar surface; these magnitudes again exceeded the ultimate strength of 7 MPa for the medial femoral cartilage [47], shown in Fig. 22 A), thereby confirming susceptibility to cartilage degradation on that side.

Table 2: Comparison of peak von-Mises stress (MPa) and ultimate strength (MPa) for the knee constituents in the neutral, varus and valgus models, with L = lateral compartment, M = medial compartment, UTS = ultimate tensile strength, UCS = ultimate compressive strength.

Knee Constituent	**Von-Mises stress (MPa)**								**Ultimate Stress (MPa)**
	+15°	+10°	+5°	0°	-3.5°	-5°	-10°	-15°	
Femur Bone	2.183	2.176	2.188	2.193	2.195	2.199	2.591	2.56	UCS 10.16 [46]
Femur Bone (cortical)	147.058	147.015	144.801	129.329	120.185	116.108	139.397	147.072	UCS 200 [45]
Femoral Cartilage	**40.763(L)**	**162.173(L)**	**44.493(L)**	**13.19(L)**	**7.032(L)**	**8.212(L)**	**41.487(L)**	**30.643(L)**	UTS 7(M)/11(L) [47]
Lateral Meniscus	**31.812**	**32.467**	**30.356**	**31.753**	**24.221**	11.071	9.193	5.161	UTS 12.53 [48]
Medial Meniscus	0.802	1.225	1.256	1.556	**17.579**	13.165	**15.789**	7.351	UTS 13.215 [48]
Tibial Cartilage	0.987 (L)	1.181 (L)	1.07 (L)	0.744 (L)	1.113 (L)	1.233 (M)	2.045 (M)	2.195 (M)	UTS 8(M)/9(L) [47]
Tibia Bone (trabecular)	0.464	0.574	0.615	0.586	1.034	0.957	0.591	0.344	UCS 10.16 [46]
Tibia Bone (cortical)	18.061	21.339	47.473	26.082	147.006	78.551	146.42	38.477	UCS 200 [45]

The spatial assessment of the VMS distribution across the entire meniscal geometry, shown in Fig. 14, revealed a colour gradation from 0 to 3 MPa, with the colour-scale maxima consistently localised to the posterior-horn regions of the respective menisci across all alignment configurations. Under the neutral and valgus conditions, the peak stress concentrations were consistently localised to the posterior horn of the lateral meniscus, attaining magnitudes of approximately 31 MPa, which exceeded the reported ultimate tensile strength of 12.53 MPa for the lateral meniscus [48], shown later in Fig. 22 B), thereby indicating a pronounced susceptibility to damage initiation across all angulation severities, including the neutral condition. In the varus series the stress shifted to the medial meniscus, with the peak magnitudes observed on its posterior horn remaining well below those of the neutral and valgus models. The -10° configuration produced peak magnitudes that surpassed the ultimate tensile strength of the medial meniscus [48], rendering it susceptible to damage initiation, as also shown in Fig. 22 C).

Fig. (15) shows the VMS distributions across the tibial cartilage under the neutral, valgus and varus conditions. The peak magnitudes remained below 2.2 MPa for all angulations, considerably lower than those recorded in the other knee soft tissues, namely the femoral cartilage and meniscus, indicating the comparatively lower mechanical burden borne by the tibial cartilage under the imposed loading. Under the neutral condition and consistently across the valgus series, the lateral tibial cartilage retained its stress-concentration pattern, with colour-scale maxima of 0.744 MPa at 0°, increasing progressively from 1.070 MPa at $+5^{\circ}$ to a peak of approximately 1.181 MPa at $+10^{\circ}$, followed by a marginal decrease to 0.987 MPa at $+15^{\circ}$, while the medial tibial cartilage retained near-negligible stress magnitudes. In the varus series, a reorganised stress distribution was observed, with the dominant concentration moving entirely from the lateral to the medial tibial cartilage, the colour-scale maxima increasing progressively from approximately 1.233 MPa at -5° to 2.045 MPa at -10° and reaching a global maximum of approximately 2.195 MPa at -15°. The peak VMS for all angulations in both series remained well within the reported ultimate strength thresholds of 9 MPa for the lateral tibial cartilage [47] and 8 MPa for the medial tibial cartilage [47], indicating that damage initiation is unlikely in this constituent.

For the tibia bone, the predominant stress field across the bulk of the tibial plateau

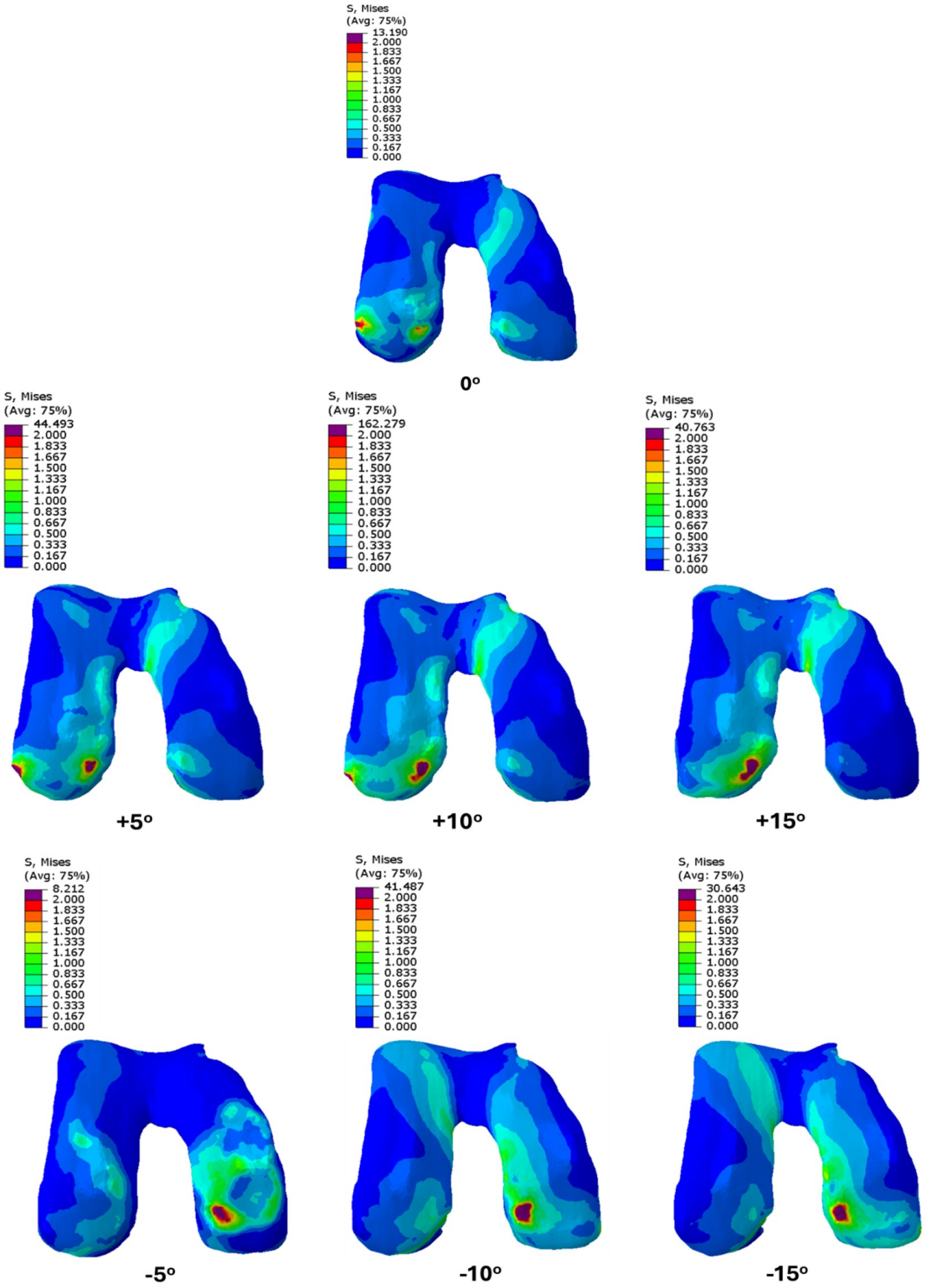


Figure 13: Three-dimensional contour plots of the von-Mises stress distribution in the femoral cartilage across both compartments, with peaks on the lateral compartment in the neutral (0°) and valgus (+5°, +10°, +15°) models and on the medial compartment in the varus (−5°, −10°, −15°) models.

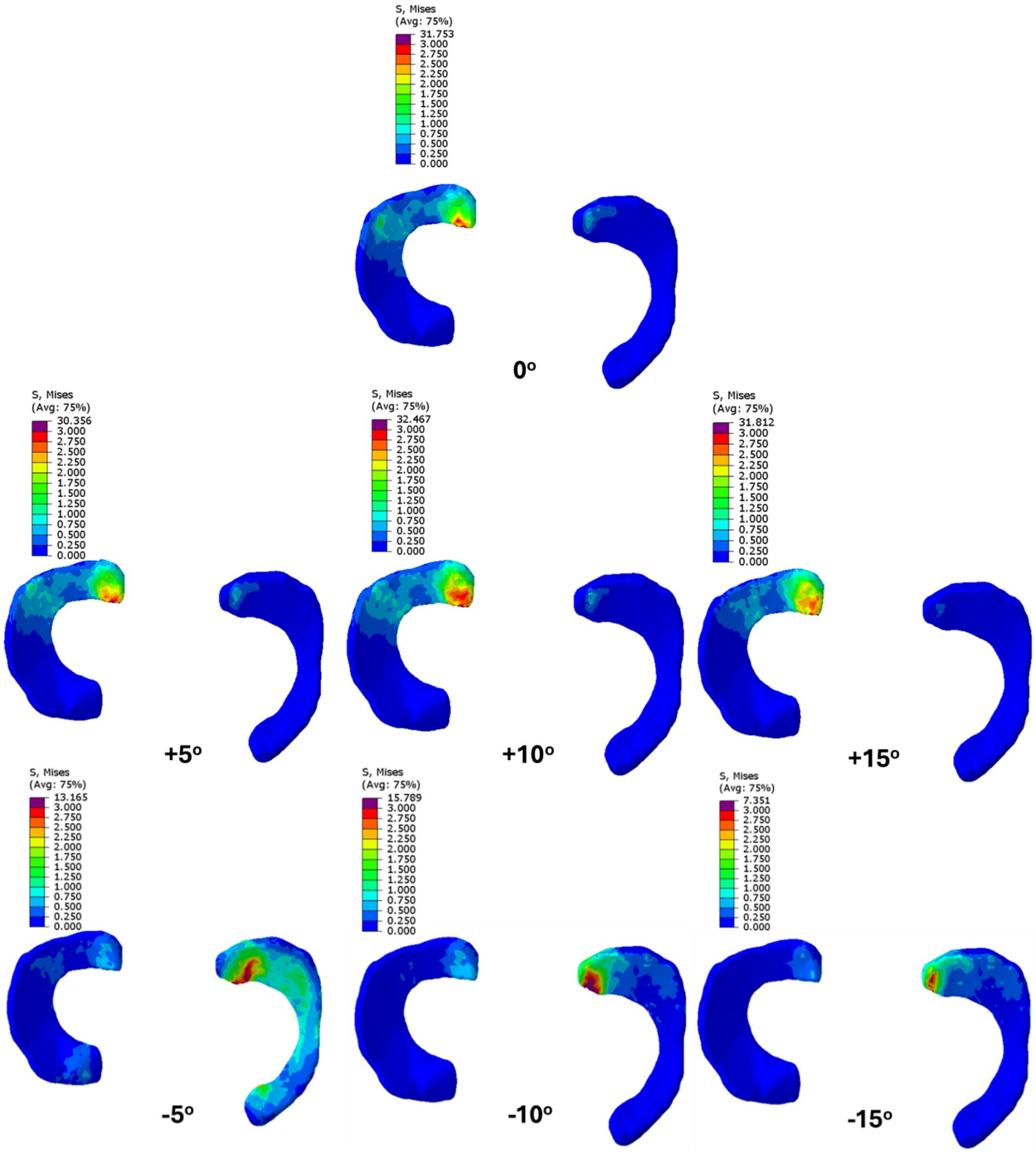


Figure 14: Three-dimensional contour plots of the von-Mises stress distribution in the meniscus, localised to the posterior horn of the lateral meniscus in the neutral (0°) and valgus (+5°, +10°, +15°) models and to the posterior horn of the medial meniscus in the varus (−5°, −10°, −15°) models.

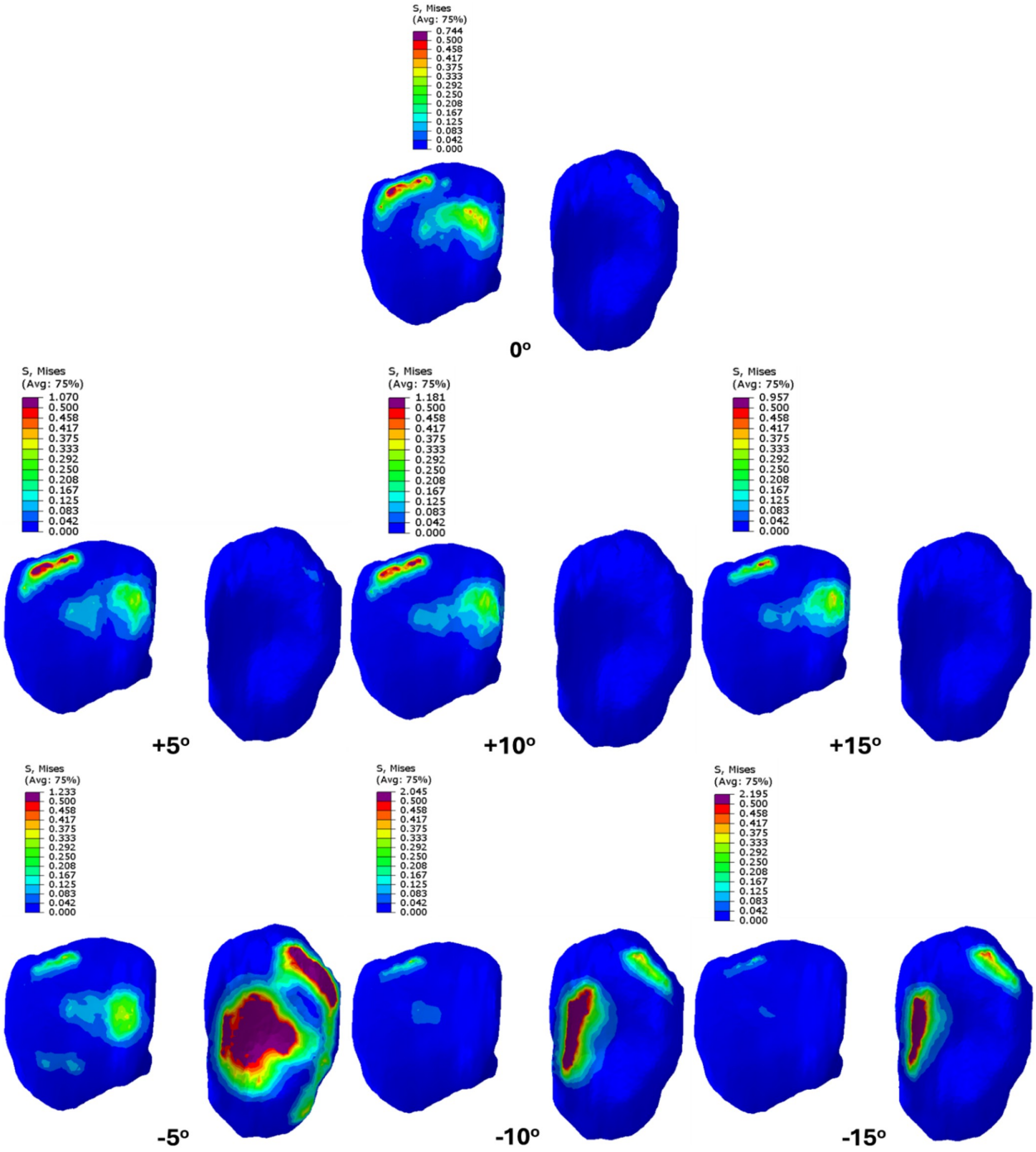


Figure 15: Three-dimensional contour plots of the von-Mises stress distribution in the tibial cartilage, localised to the lateral tibial cartilage in the neutral (0°) and valgus (+5°, +10°, +15°) models and to the medial tibial cartilage in the varus (−5°, −10°, −15°) models.

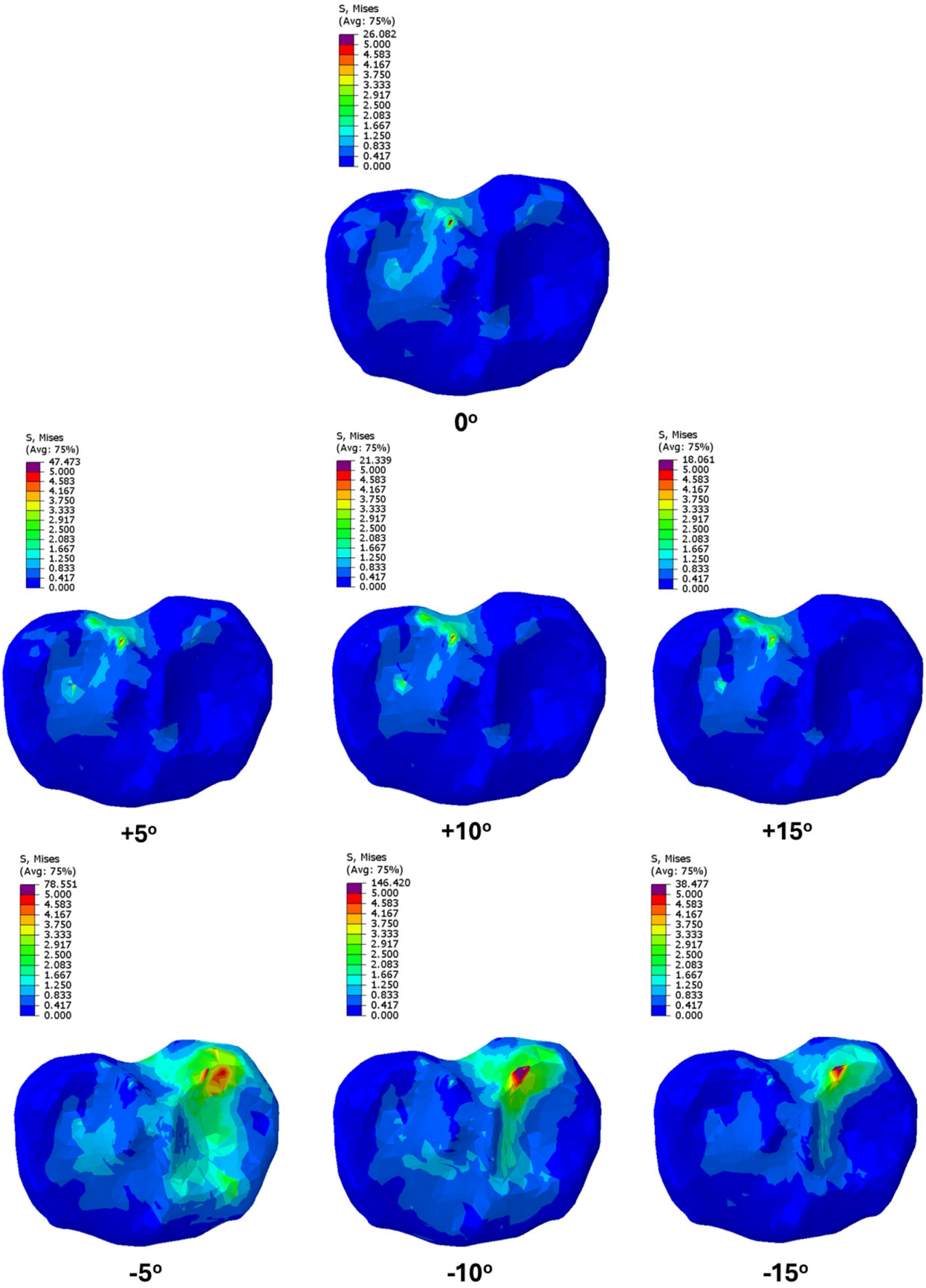


Figure 16: Three-dimensional contour plots of the von-Mises stress distribution in the tibia bone, localised to the lateral compartment in the neutral (0°) and valgus (+5°, +10°, +15°) models and to the medial compartment in the varus (−5°, −10°, −15°) models.

surface remained below 5 MPa for all angulation conditions, as shown in Fig. 16. In the neutral condition and the entire valgus series, the lateral tibial plateau retained its role as the dominant stress-concentration site, with colour-scale maxima of approximately 26.082 MPa at 0°, increasing to 47.473 MPa at +5°, followed by progressive attenuation to approximately 21.339 MPa at +10° and 18.061 MPa at +15°. For the varus configurations, the stress redistributed from the lateral to the medial tibial plateau, with an abrupt increase in both spatial extent and magnitude from 78.551 MPa at −5° to a global maximum of 146.420 MPa at −10°, followed by a reduction to 39.477 MPa at −15°. Critically, the peak stresses across the range of malalignment severities investigated remained well within the reported ultimate compressive stress threshold of 200 MPa for cortical bone [45] and 10.16 MPa for trabecular bone [46], indicating a low likelihood of damage initiation in the proximal tibia.

To examine whether even modest varus angulations within the range of −1° to −4° can impose substantially elevated peak VMS concentrations on the knee constituents, and thereby help resolve the clinical question of whether such minor deviations warrant treatment, the stresses in the corresponding models were analysed, as summarised in Table 3.

As shown in Fig. (17), when the VMS was evaluated across varus angles from −1° to −4° for the femur bone, the stress concentrations were found to be more pronounced on the lateral postero-superior surface, a pattern consistent with that observed in the valgus models of Fig. (12), while the articular surface continued to bear the least stress. Although the colour-scale maxima across all four configurations ranged from approximately 118 to 147 MPa, approaching but not exceeding the ultimate strength threshold of 200 MPa reported for cortical bone, the −1° and −4° configurations attained the highest peak of approximately 147 MPa.

As shown in Fig. 18, the VMS distribution in the femoral cartilage spanned both the lateral and medial compartments, a pattern analogous to that recorded in the varus models of Fig. 13. The peak VMS were localised within the lateral compartment of the femoral cartilage for the −1° and −2° angles, with the −1° model exhibiting the highest magnitude of approximately 21 MPa. The medial femoral cartilage, departing from the classical biomechanical expectation of medial overloading in varus-aligned knees, exhibited comparatively lower stress magnitudes in the mild angulation range examined. The observed peak stresses

Table 3: Comparison of peak von-Mises stress (MPa) and ultimate strength (MPa) for the knee constituents in the varus models (-1°, -2°, -3°, -4°); L = lateral compartment, M = medial compartment, UTS = ultimate tensile strength, UCS = ultimate compressive strength.

Knee Constituent	**von-Mises stress (MPa)**				**Ultimate Strength (MPa)**
	-1°	-2°	-3°	-4°	
Femur Bone (trabecular)	2.435	2.304	2.182	2.193	UCS 10.16 [46]
Femur Bone (cortical)	147.069	123.263	118.7	147	UCS 200 [45]
Femoral Cartilage	**21.356 (L)**	9.032 (L)	**9.802 (M)**	**7.976 (M)**	UTS 7(M)/11(L) [47]
Lateral Meniscus	**32.156**	**30.958**	**27.024**	**18.46**	UTS 12.53 [48]
Medial Meniscus	1.783	1.806	**17.636**	**17.75**	UTS 13.215 [48]
Tibial Cartilage	0.968 (L)	1.293 (L)	1.134 (L)	1.06 (L)	UTS 8(M)/9(L) [47]
Tibia Bone (trabecular)	0.529	0.854	0.798	1.029	UCS 10.16 [46]
Tibia Bone (cortical)	27.497	125.76	146.96	108.3	UCS 200 [45]

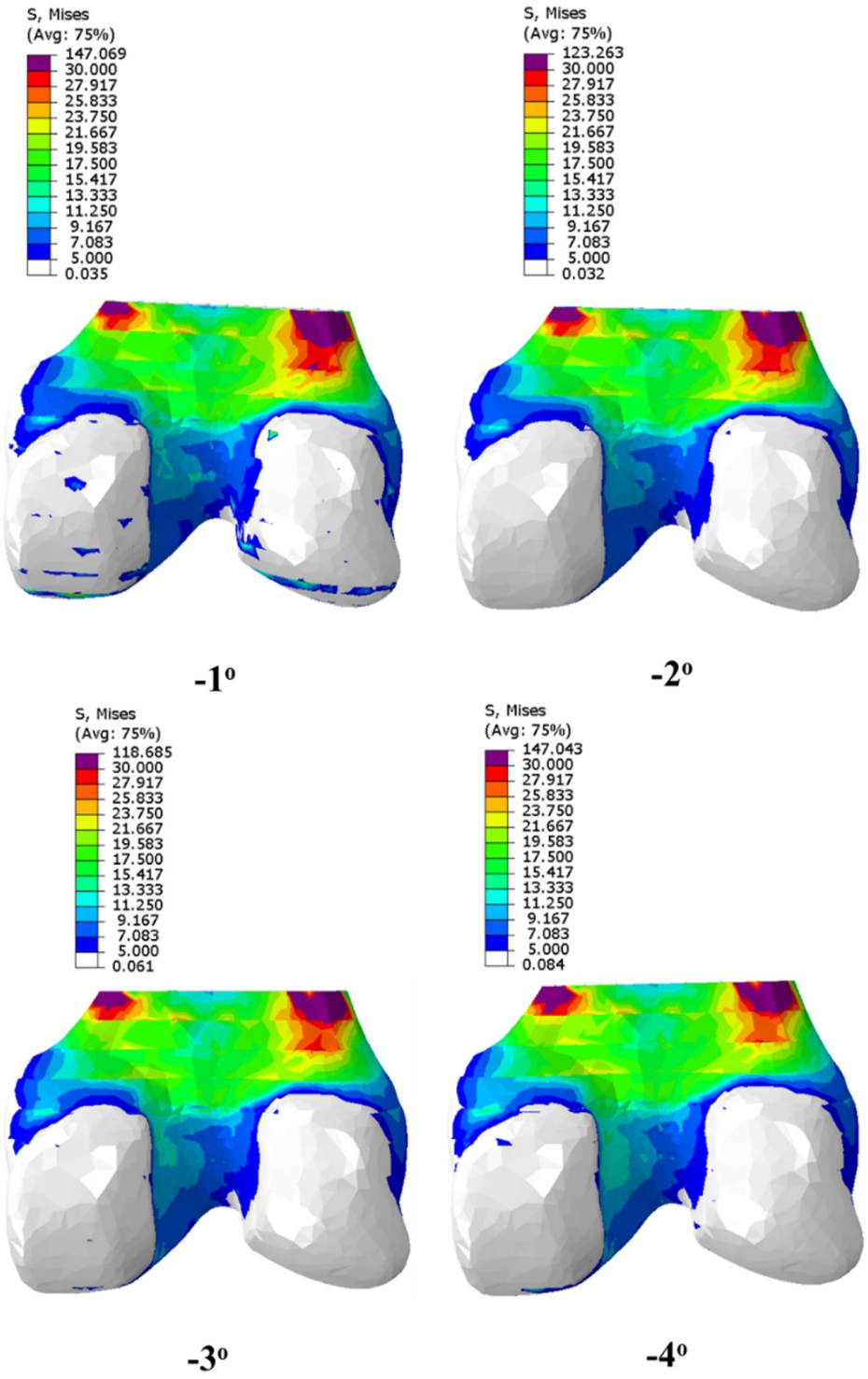


Figure 17: Three-dimensional contour plots of the von-Mises stress distribution in the femur bone, localised to the lateral postero-superior surface for the varus ($-1°$, $-2°$, $-3°$, $-4°$) models in the posterior view.

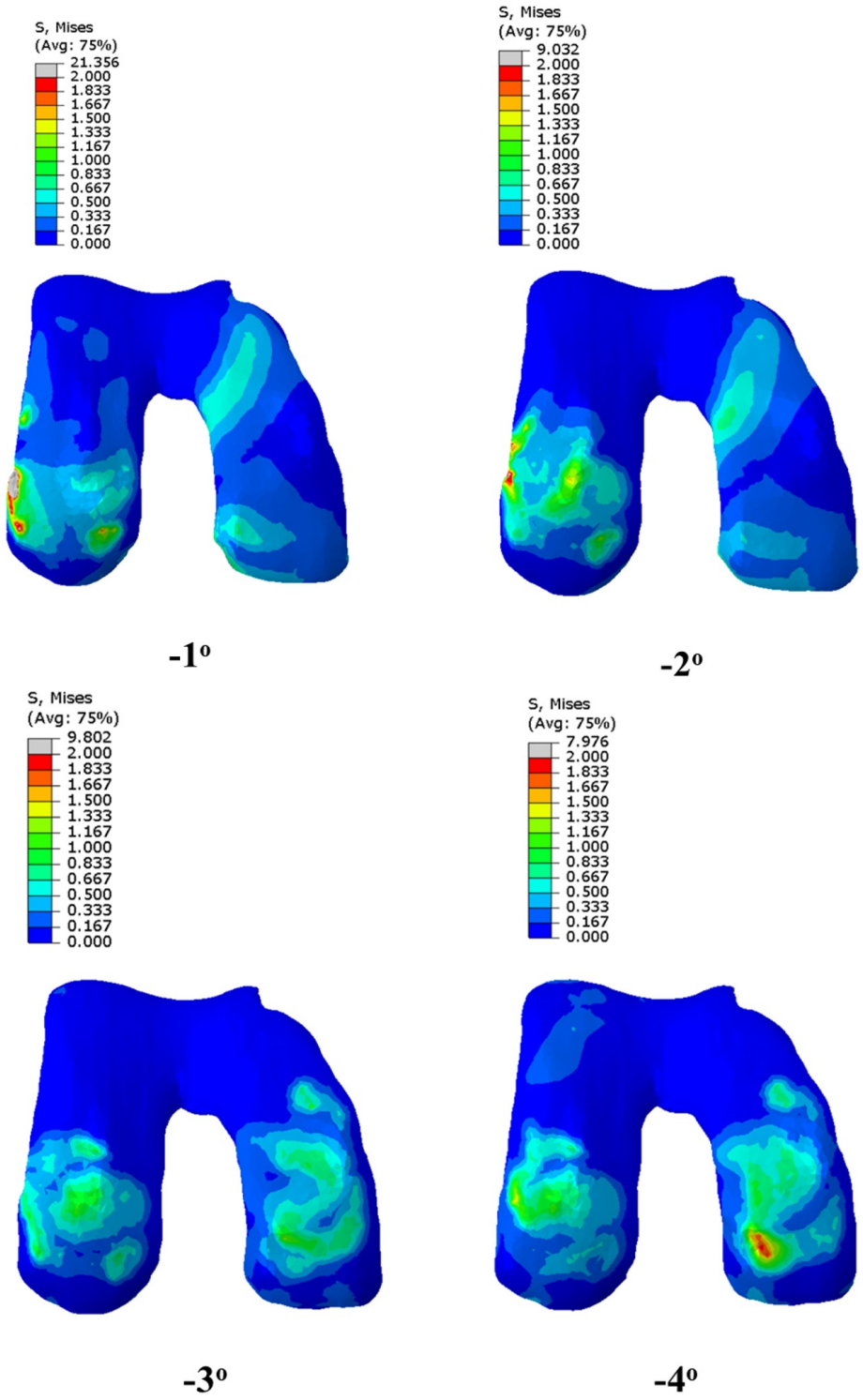


Figure 18: Three-dimensional contour plots of the von-Mises stress distribution in the femoral cartilage across both compartments, with peaks on the lateral compartment for varus $-1°$ and $-2°$ and on the medial compartment for varus $-3°$ and $-4°$.

surpassed the ultimate strength threshold of 11 MPa reported for the lateral femoral cartilage [47], shown in Fig. 22 A), at $-1°$, and the threshold of 7 MPa reported for the medial femoral cartilage [47] in the $-3°$ and $-4°$ configurations, indicating susceptibility to tissue failure.

Fig. 19 shows the three-dimensional contour plots of the VMS distribution in the meniscus across the mild varus angulations. Stress concentrations were distributed over the lateral meniscus for all four configurations from $-1°$ to $-4°$, while the $-3°$ and $-4°$ configurations additionally exhibited elevated stress over both the lateral and medial menisci. Damage susceptibility was observed on the lateral meniscus across all configurations, as the recorded peak VMS exceeded the ultimate strength of 12.53 MPa reported for the lateral meniscus [48], shown later in Fig. 22 B). Furthermore, the ultimate strength threshold of 13.215 MPa corresponding to the medial meniscus [48] was also surpassed in the $-3°$ and $-4°$ configurations, shown in Fig. 22 C), indicating increased susceptibility to structural damage within the medial meniscus at the higher varus angulations.

As shown in Fig. 20, the VMS distribution in the tibial cartilage was evaluated across the acute varus configurations, recording peak magnitudes from 0.968 to 1.293 MPa, all of which remained below the ultimate strength threshold. At $-1°$, the stress concentrations were localised at the periphery of the lateral tibial plateau, progressively transitioning into a more centrally distributed high-stress zone with increasing varus angulation. At $-3°$ and $-4°$, the medial tibial plateau also began to display elevated stress, indicating bicompartmental involvement. The tibia bone showed higher VMS in the lateral tibial plateau, increasing from 27.497 MPa at $-1°$ to 125.760 MPa at $-2°$, as observed in Fig. 21. As the angulation increased, the medial compartment also developed elevated stress, with peaks of 146.968 MPa at $-3°$ and 108.266 MPa at $-4°$. The stresses for all angulations remained well within the 200 MPa ultimate strength limit for cortical bone.

This study identifies the femoral cartilage and the meniscus as the primary potential sites of damage initiation, a finding consistent with the previous studies summarised in Table 4, across nearly all valgus and varus configurations examined. While those studies additionally identified the medial tibial cartilage as a damaged structure under varus conditions, this discrepancy may be attributable to the ligament modelling incorporated in those investigations,

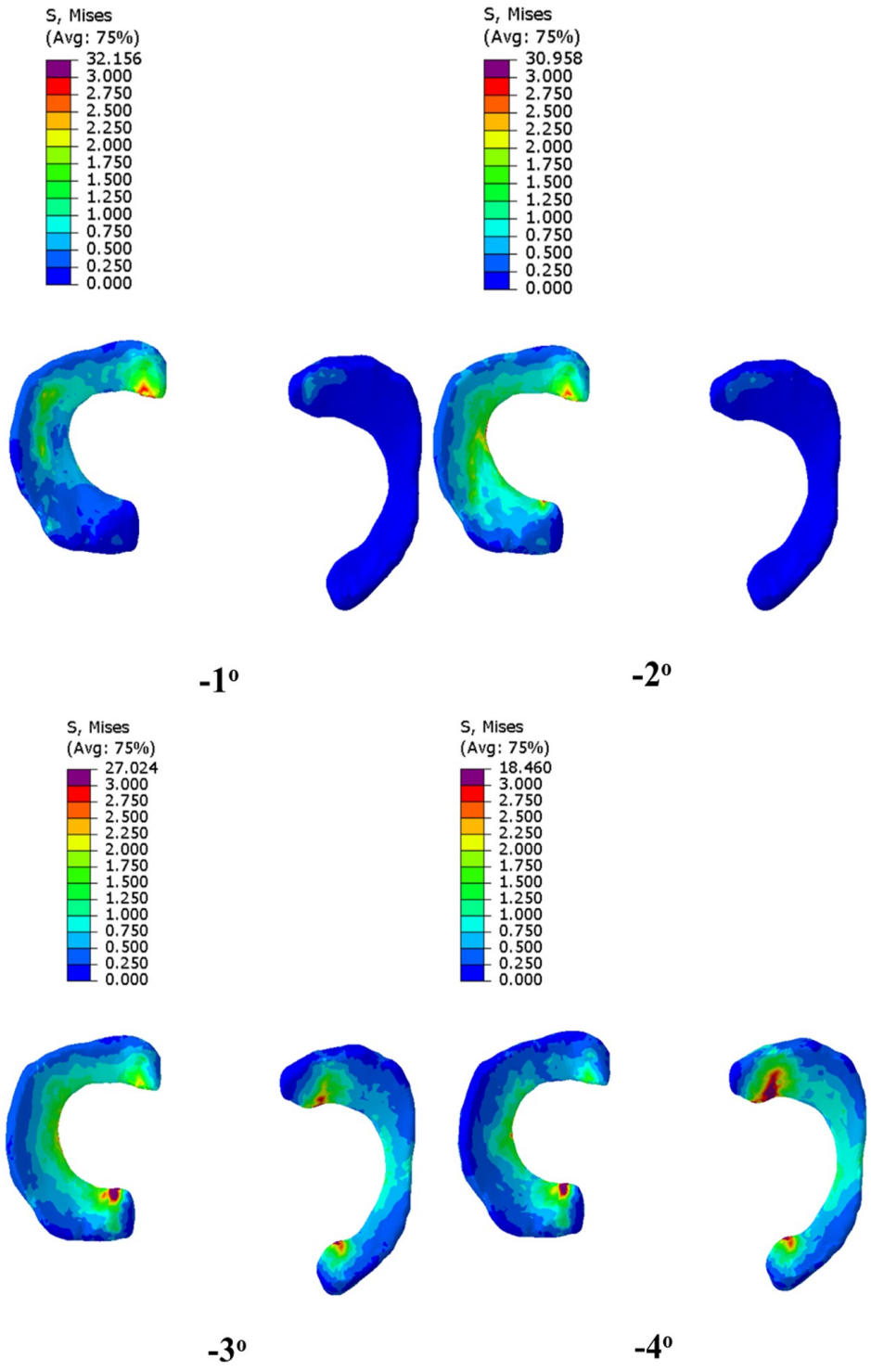


Figure 19: Three-dimensional contour plots of the von-Mises stress distribution in the menisci, observed on the lateral meniscus for varus $-1°$ and $-2°$ and on both the lateral and medial menisci for varus $-3°$ and $-4°$, with peaks on the medial compartment.

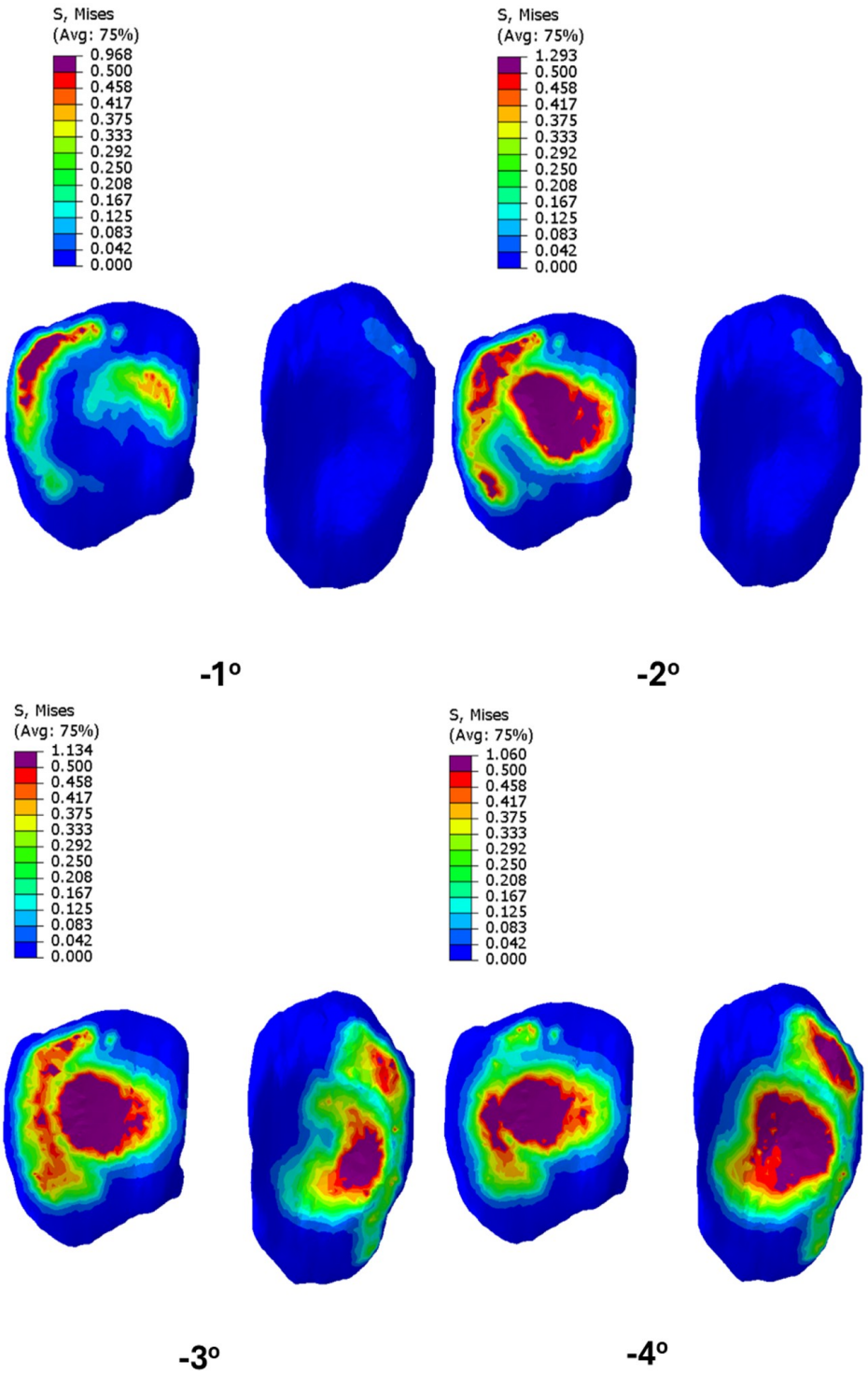


Figure 20: Three-dimensional contour plots of the von-Mises stress distribution in the tibial cartilage, localised to the lateral tibial cartilage for varus $-1°$ and $-2°$ and across both the lateral and medial tibial cartilage for varus $-3°$ and $-4°$, with peaks on the medial tibial cartilage.

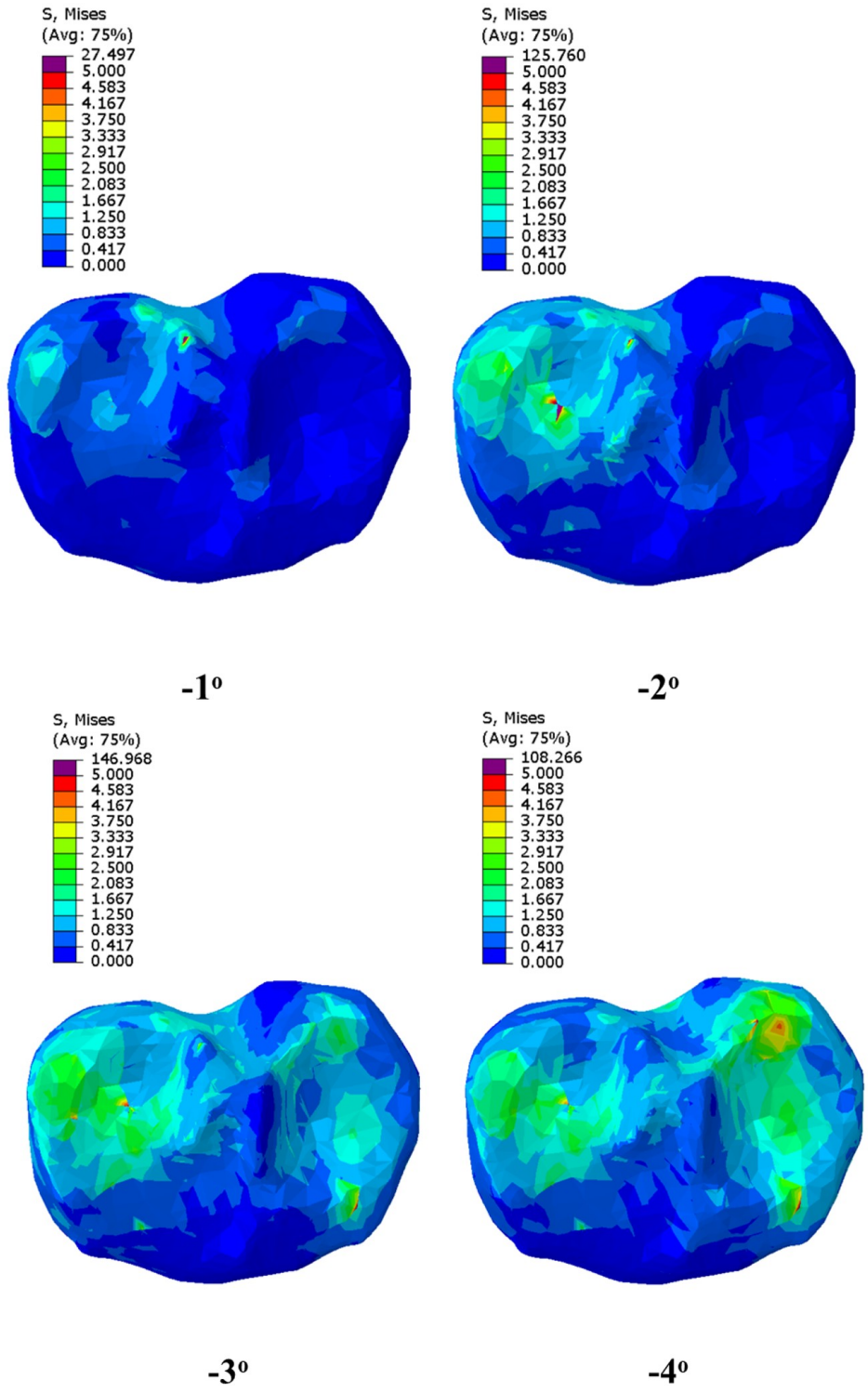


Figure 21: Three-dimensional contour plots of the von-Mises stress distribution in the tibia bone, localised to the lateral tibial plateau for varus $-1°$ and $-2°$ and across both the lateral and medial tibial plateau for varus $-3°$ and $-4°$, with peaks on the medial tibial plateau.

Table 4: Numerical and clinical studies reporting the damaged knee components for varus and valgus angles under different loading conditions.

Angles	**Damaged Knee Component**	**Load**	**Numerical/ Clinical results**	**Citation**
0°–18° Varus with 3° increments	*Medial Tibial Cartilage*	740 N	Numerical	Zhang H, et al. 2024 [26]
0°–12° Varus with 4° increments	Femoral Cartilage, *Medial Tibial Cartilage*, Medial Meniscus	500–1250 N	Numerical	Trad Z, et al. 2017 [33]
Mean Varus angle 7.17°–1.32° with mild knee OA	Femoral Cartilage, *Medial Tibial Cartilage*	750 N	Numerical	Pan D, et al. 2020 [49]
1°–3° Valgus, >3° Valgus	Lateral Articular Cartilage, Lateral Meniscus	Natural Body weight of patients	Clinical	Felson D.T, et al. 2013 [9]
2° Valgus 2° Varus	Lateral Meniscus, Medial Meniscus, *Medial Tibial Cartilage*	1620 N	Numerical	Haris A, et al. 2020 [50]

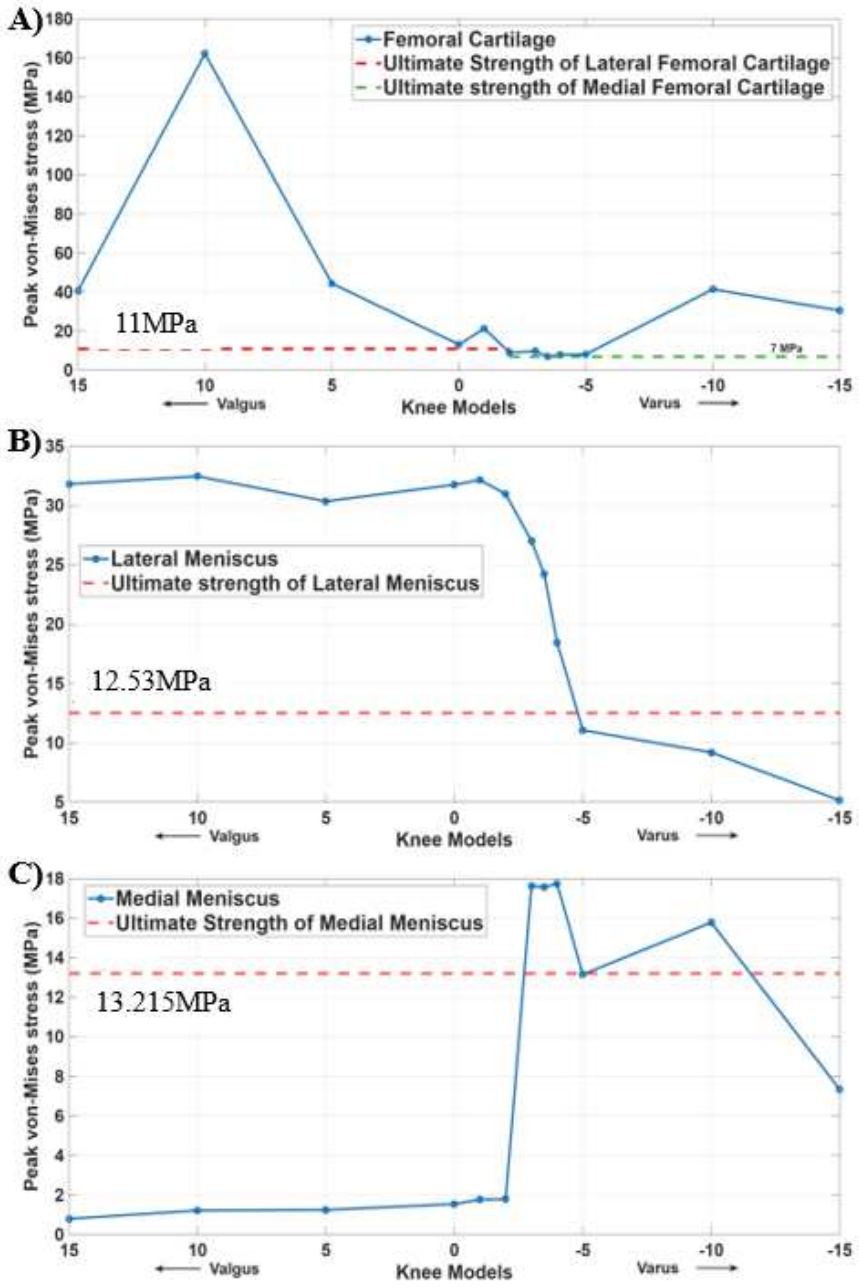


Figure 22: Comparison of peak von-Mises stress (MPa) with the ultimate strength (MPa) for A) the femoral cartilage, B) the lateral meniscus and C) the medial meniscus across the valgus and varus configurations; a component is identified as damaged for a given angle when its peak stress surpasses the corresponding ultimate strength.

an element absent from the present model, which likely conferred greater structural stability and consequently facilitated enhanced load transfer to that tissue. Whether the inclusion of ligament modelling in future iterations of this study would yield analogous results for the medial tibial cartilage represents an avenue worthy of further exploration.

5. Behaviour of a crack in a hyper-elastic material in the presence of a hole

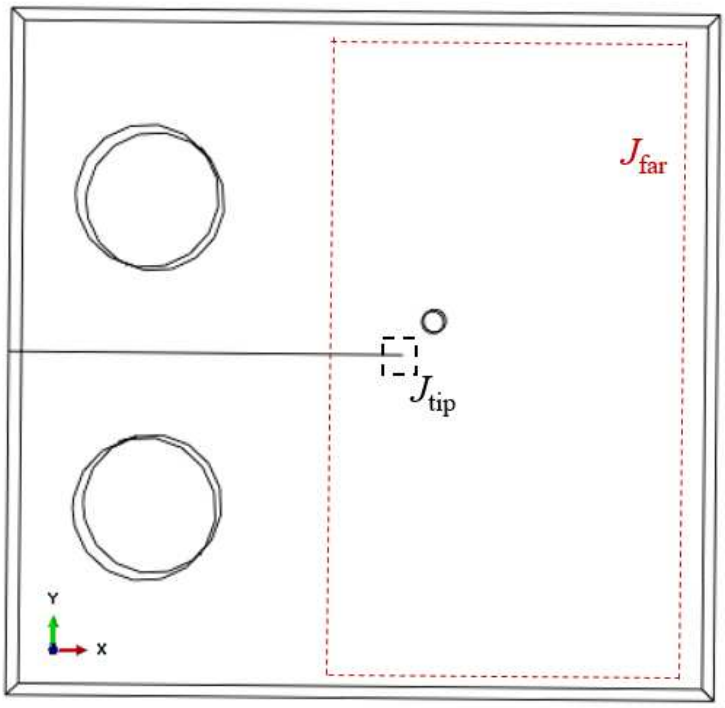


Figure 23: Three-dimensional CT specimen modelled with hyper-elastic properties and a hole, showing the selected contours.

From the foregoing observations, it can be concluded that the cartilage, modelled as a hyper-elastic material, shows a comparatively higher tendency towards damage initiation than the other knee joint constituents. Therefore, to further investigate the fracture behaviour of the hyper-elastic cartilage material and to examine the influence of a nearby hole on crack behaviour, a three-dimensional Compact Tension (CT) specimen was modelled. The specimen has a width of 25 mm and a thickness of 3.125 mm. An initial crack length of 11.25 mm is introduced, together with a circular hole of radius 0.5 mm positioned at a horizontal distance of 1.375 mm and a vertical distance of 1.5 mm from the crack tip, as

shown in Fig. (23). The near-tip contour (J_{tip}) and far-field contour (J_{far}) were selected as shown in Fig. (23), and the same contours were extended throughout the thickness of the specimen. A mesh size of 0.05×0.05 mm^2 was used to resolve the stress fields close to the crack tip. The selected contours were used to evaluate the configurational forces at the crack tip and to predict the expected crack growth direction throughout the specimen thickness. The same hyper-elastic material properties assigned to the femoral cartilage were used for the CT specimen model in Abaqus, and the corresponding schematic stress-strain behaviour is shown in Fig. (24).

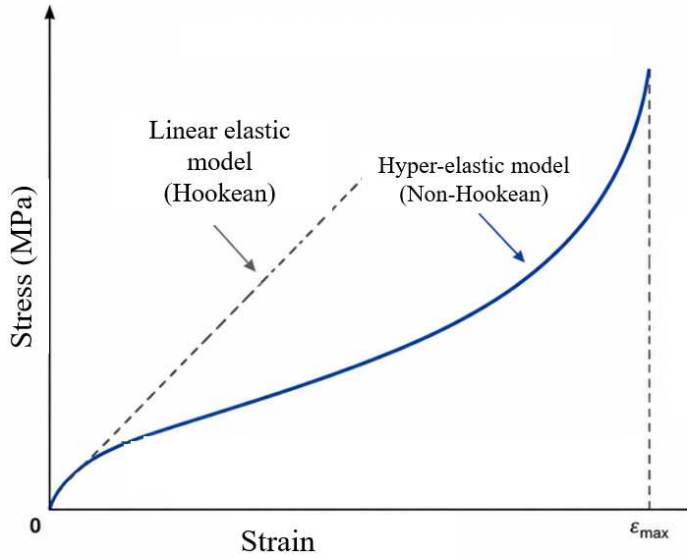


Figure 24: Schematic of the stress-strain behaviour of the hyper-elastic material.

To interpret the fracture behaviour investigated here, it is useful to introduce the concept of configurational forces. Configurational forces are thermodynamic driving forces associated with the initiation and evolution of material defects such as cracks, voids, dislocations and interfaces. In fracture mechanics they play a central role in predicting crack growth and the energetically favourable crack growth direction. In this study, a configurational-force-based J-integral approach is used to investigate the fracture behaviour of the hyper-elastic material in the presence of a hole. Unlike the conventional J-integral, which is mainly applicable to homogeneous materials under proportional loading, the configurational-force framework can also account for material and geometric inhomogeneities. It is therefore particularly suitable for analysing the interaction of a crack with inhomogeneities such as holes, where the crack

driving force may either increase or decrease depending on the local stress redistribution around the defect.

The bulk configurational force, denoted by $\mathbf{f}$, can be expressed as

$$\mathbf{f} = -\nabla \cdot \left(\phi \mathbf{I} - \mathbf{F}^T \mathbf{S}\right) \tag{4}$$

where $\nabla\cdot$ is the divergence operator, ϕ is the strain energy density, $\mathbf{I}$ is the identity tensor, $\mathbf{F}^T$ is the transpose of the deformation gradient tensor, and $\mathbf{S}$ is the first Piola-Kirchhoff stress tensor. The configurational force thus represents the material force arising from spatial variations in the strain energy field. The scalar value of the J-integral can be evaluated from the configurational forces projected along the expected crack growth direction as

$$J_\Gamma = \mathbf{e} \cdot \sum \left(-\mathbf{f}_\Gamma\right) \tag{5}$$

where $\mathbf{e}$ is the unit vector along the expected crack propagation direction and $\mathbf{f}_\Gamma$ represents the configurational forces enclosed within the selected contour region. The above expression can be used to evaluate the J-integral components along both the x- and y-directions, denoted J^x and J^y respectively. In this study, the near-tip contour (J_{tip}) and far-field contour (J_{far}) are evaluated to investigate the crack driving force in the presence of the hole. The expected crack growth direction, θ, can be evaluated from the ratio of the configurational force components in the y- and x-directions, i.e.

$$\theta = \tan^{-1}\left(\frac{J^y}{J^x}\right) \tag{6}$$

For a more detailed treatment of configurational forces, the reader is referred to Kolednik et al. [51].

After the simulation, the configurational force vectors obtained from two different views are shown in Fig. (25), and the corresponding crack propagation angle, θ, is evaluated. The ratio $J_{\text{tip}}/J_{\text{far}}$ was found to be greater than unity, indicating that the crack exhibits a tendency to be attracted towards the hole. This behaviour is consistent with previous studies of crack-hole interaction using configurational-force-based analysis [52]. The variation of θ with J_{far} at the surface of the CT specimen is shown in Fig. (26). With increasing J_{far},

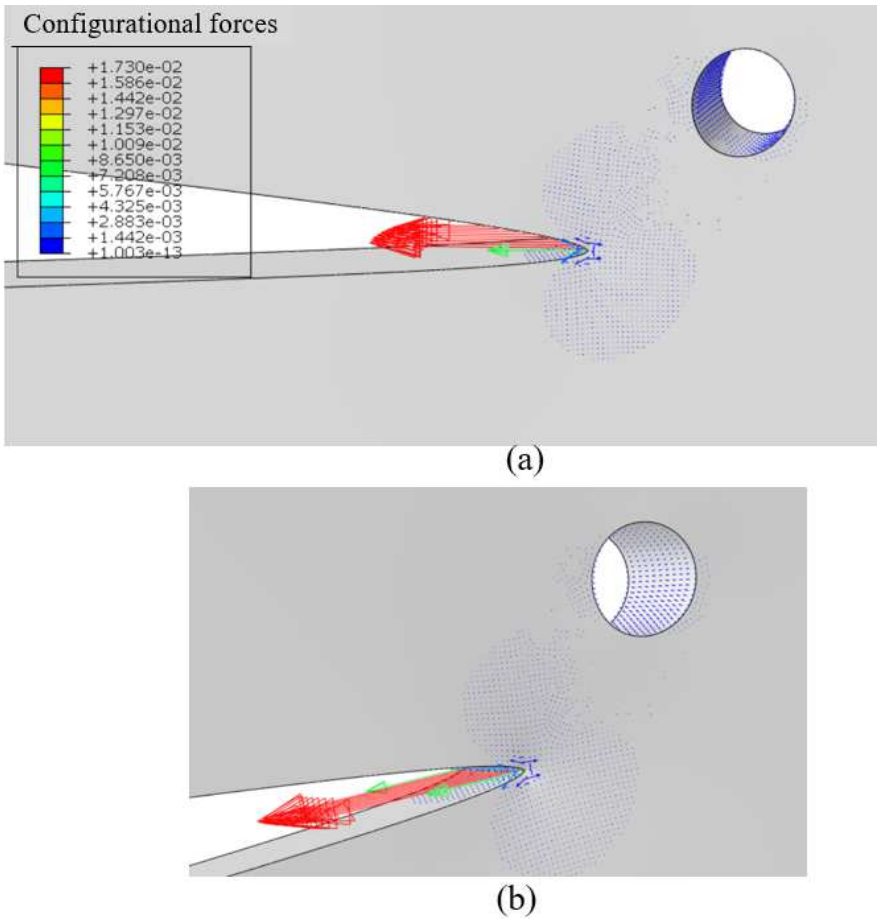


Figure 25: Symbolic representation of the configurational forces at the crack tip in the presence of a hole, shown from two different views.

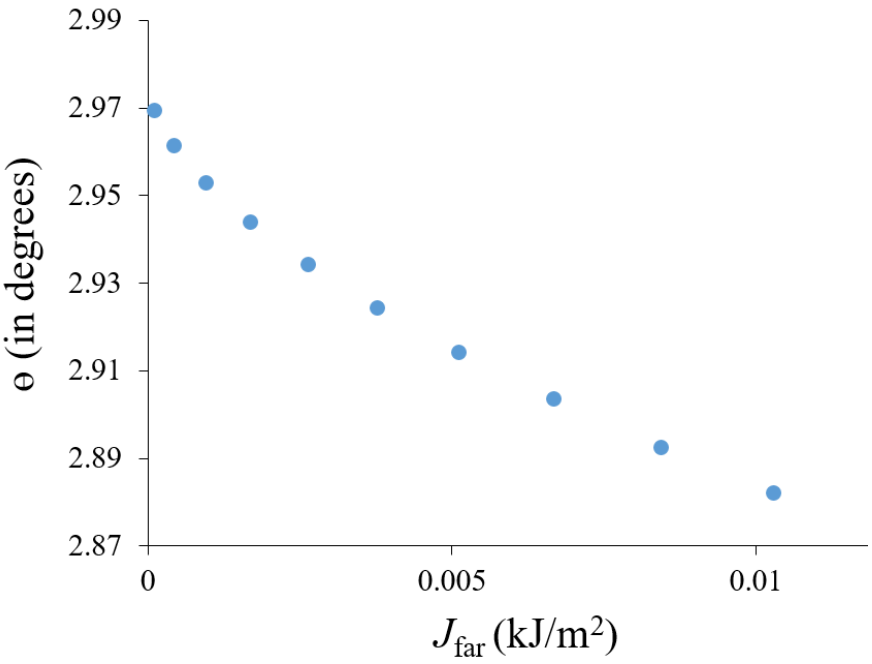


Figure 26: Variation of θ (°) with J_{far} at the surface of the three-dimensional CT specimen.

the expected crack propagation angle decreases, indicating that the nearby hole significantly influences both the crack driving force and the crack trajectory in the hyper-elastic material. The reduction in crack propagation angle reflects a tendency of the crack path to reorient towards a comparatively stable propagation direction owing to the stress redistribution around the hole. This behaviour highlights the strong sensitivity of hyper-elastic materials to geometric discontinuities, where the local deformation field surrounding the hole modifies the configurational-force distribution and consequently alters the crack growth behaviour.

The variation of the crack propagation angle, θ, along the thickness of the CT specimen, d, was also evaluated from the surface towards the centre for the final displacement value, as shown in Fig. (27). The crack propagation angle has its maximum value at the free surface and decreases gradually along the thickness direction, becoming nearly stable towards the central region of the specimen. Near the free surface, the material experiences comparatively lower constraint and larger deformation, which leads to higher configurational-force components in the transverse direction and hence to larger crack deflection angles. Towards the interior of the specimen, the deformation state becomes more constrained by the surrounding material, resulting in a comparatively stable stress and strain field; as a result, the

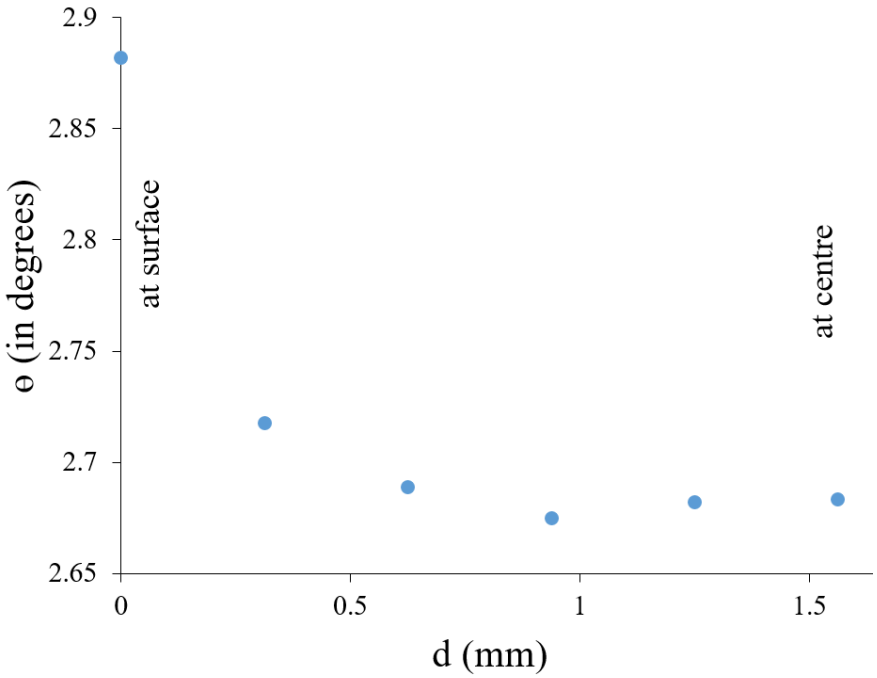


Figure 27: Variation of θ (°) with distance from the surface to the centre of the CT specimen.

crack propagation direction gradually stabilises near the centre of the CT specimen along the thickness. This variation further demonstrates the strong influence of three-dimensional hyper-elastic deformation on the crack growth behaviour in the presence of holes.

6. Conclusion

The present study reveals a notable asymmetry in both the spatial distribution and the peak magnitude of the von-Mises stress (VMS) across the simulated varus and valgus models, reflecting differential stress redistribution in response to varying severities of imposed malalignment. The VMS within the femoral cartilage consistently exceeded the ultimate strength threshold, confirming structural failure of the tissue. This degradation manifested predominantly in the lateral compartment under valgus and neutral alignment, as well as at varus malalignment up to $-1°$; in contrast, varus malalignment of $-3°$ and beyond selectively predisposed the medial compartment to mechanical compromise. Correspondingly, the lateral meniscus demonstrated progressive structural deterioration with escalating valgus deformity, persisting through neutral alignment and extending into varus malalignment up to $-4°$. Similarly, the medial meniscus exhibited marked vulnerability to failure at varus

angles of -3° to -4°, with a recurrence at -10°. Several limitations of this study must be acknowledged. First, the knee geometry of only one patient was used to construct all the valgus and varus models, which restricts the generalisability of the findings, as physiological alignment, joint curvature and dimensions are specific to each individual. Second, key anatomical structures, including the muscles, ligaments, fibula and patella, were excluded to reduce the computational load. Third, only a single-limb standing simulation was performed; the dynamic loading conditions encountered during gait were not considered. Collectively, these simplifications may contribute to either an underestimation or an overestimation of the reported VMS values. Finally, the behaviour of a crack in the presence of a hole in a hyper-elastic material was investigated using configurational forces, revealing the influence of the hole on the expected crack direction, including its variation along the thickness. Future studies should therefore incorporate knee geometries from a larger patient cohort and include critical structures such as the ligaments and muscles to improve joint stability, as well as extend the analysis to capture dynamic loading conditions.

Acknowledgements

This work was supported by the Indian Institute of Technology Ropar, Punjab, India. The authors acknowledge the support of the Institute.

Conflicts of interest/Competing interests

The authors have no conflicts of interest to declare that are relevant to the content of this article.

Data Availability statement

The authors confirm that the data supporting the findings of this study will be made available on request to the corresponding author.

References

[1] F. Flandry and G. Hommel, "Normal anatomy and biomechanics of the knee," *Sports Medicine and Arthroscopy Review*, vol. 19, no. 2, pp. 82–92, 2011.

[2] D. K. Ramsey and P. F. Wretenberg, "Biomechanics of the knee: methodological considerations in the in vivo kinematic analysis of the tibiofemoral and patellofemoral joint," *Clinical Biomechanics*, vol. 14, no. 9, pp. 595–611, 1999.

[3] V. Coppa *et al.*, "Coronal plane deformity around the knee in the skeletally immature population: A review of principles of evaluation and treatment," *World Journal of Orthopedics*, vol. 13, no. 5, pp. 427–443, 2022.

[4] M. Patel and R. Nelson, "Genu valgum," in *StatPearls*. Treasure Island (FL): StatPearls Publishing, 2026.

[5] N. Marques Luís and R. Varatojo, "Radiological assessment of lower limb alignment," *EFORT Open Reviews*, vol. 6, no. 6, pp. 487–494, 2021.

[6] C. Suardi *et al.*, "Varus morphology and its surgical implication in osteoarthritic knee and total knee arthroplasty," *Journal of Orthopaedic Surgery*, vol. 17, no. 1, p. 299, 2022.

[7] J. An *et al.*, "Deformity in valgus knee malalignment is not only in the femur but also in tibia or both, based on demographic and morphological analysis before and after knee osteotomies," *Knee Surgery, Sports Traumatology, Arthroscopy*, vol. 32, no. 4, pp. 1087–1095, 2024.

[8] S. M. J. Mortazavi, A. Noori, F. Vosoughi, R. Rezaei Dogahe, and M. J. Shariyate, "Femur originated genu varum in a patient with symptomatic acl deficiency: a case report and review of literature," *BMC Musculoskeletal Disorders*, vol. 22, no. 1, p. 437, 2021.

[9] D. T. Felson *et al.*, "Valgus malalignment is a risk factor for lateral knee osteoarthritis incidence and progression: Findings from the multicenter osteoarthritis study and the osteoarthritis initiative," *Arthritis & Rheumatism*, vol. 65, no. 2, pp. 355–362, 2013.

[10] M. Rühling, S. Kirschbaum, C. Perka, and F. Graef, "Functional gait analysis reveals insufficient hindfoot compensation for varus and valgus osteoarthritis of the knee," *International Orthopaedics*, vol. 47, no. 5, pp. 1233–1242, 2023.

[11] X. Wang *et al.*, "The influence of varus and valgus deviation on the contact area of patellofemoral joint in healthy knees," *BMC Musculoskeletal Disorders*, vol. 24, no. 1, p. 857, 2023.

[12] F. Soheilipour *et al.*, "The prevalence of genu varum and genu valgum in overweight and obese patients: Assessing the relationship between body mass index and knee angular deformities: Genu varum and genu valgum in obese patients," *Acta Biomedica Atenei Parmensis*, vol. 91, 2020.

[13] S. Bout-Tabaku *et al.*, "Obesity is associated with greater valgus knee alignment in pubertal children, and higher body mass index is associated with greater variability in knee alignment in girls," *The Journal of Rheumatology*, vol. 42, no. 1, pp. 126–133, 2015.

[14] D. J. Hunter *et al.*, "Structural factors associated with malalignment in knee osteoarthritis: the boston osteoarthritis knee study," *The Journal of Rheumatology*, vol. 32, no. 11, pp. 2192–2199, 2005.

[15] I. Ogunmwonyi, A. Adebajo, and J. M. Wilkinson, "The genetic and epigenetic contributions to the development of nutritional rickets," *Frontiers in Endocrinology*, vol. 13, p. 1059034, 2022.

[16] N. A. Segal, J. M. Nilges, and W. M. Oo, "Sex differences in osteoarthritis prevalence, pain perception, physical function and therapeutics," *Osteoarthritis and Cartilage*, vol. 32, no. 8, pp. 1045–1053, 2024.

[17] T. Uehara *et al.*, "Age-related varus progression of femoral bowing and its related factors in the iwaki cohort study," *Journal of Experimental Orthopaedics*, vol. 12, no. 1, p. e70587, 2025.

[18] R. Espandar, S. M.-J. Mortazavi, and T. Baghdadi, "Angular deformities of the lower limb in children," *Asian Journal of Sports Medicine*, vol. 1, no. 1, pp. 46–53, 2010.

[19] X. Cheng, F. Liu, F. Xiong, Y. Huang, and A. C. Paulus, "Radiographic changes and clinical outcomes after open and closed wedge high tibial osteotomy: a systematic review and meta-analysis," *Journal of Orthopaedic Surgery*, vol. 14, no. 1, p. 179, 2019.

[20] C. C. Diaz *et al.*, "Outcomes of distal femoral osteotomy for valgus malalignment: A systematic review and meta-analysis of closing wedge versus opening wedge techniques," *The American Journal of Sports Medicine*, vol. 51, no. 3, pp. 798–811, 2023.

[21] G. A. S. Sidhu *et al.*, "Results of wedgeless distal femoral osteotomy for the treatment of genu valgus deformity," *Cureus*, vol. 14, no. 11, p. e31500, 2022.

[22] M. Yan *et al.*, "Model properties and clinical application in the finite element analysis of knee joint: A review," *Orthopaedic Surgery*, vol. 16, no. 2, pp. 289–302, 2024.

[23] J. Sun *et al.*, "Finite element analysis of the valgus knee joint of an obese child," *BioMedical Engineering OnLine*, vol. 15, no. 1, p. 158, 2016.

[24] Y. Wu *et al.*, "Computer-aided design of distal femoral osteotomy for the valgus knee and effect of correction angle on joint loading by finite element analysis," *Orthopaedic Surgery*, vol. 14, no. 11, pp. 2904–2913, 2022.

[25] K. Ding *et al.*, "Finite element analysis of biomechanical effects of residual varus/valgus malunion after femoral fracture on knee joint," *International Orthopaedics*, vol. 45, no. 7, pp. 1827–1835, 2021.

[26] H. Zhang *et al.*, "Analysis of cartilage loading and injury correlation in knee varus deformity," *Medicine*, vol. 103, p. e38065, 2024.

[27] C. Yu, W. Zhao, K. Liu, X. Duan, X. Gao, L. Wang, J. Liu, J. Xu, J. Zeng, G. Chen, D. Chen, G. Xing, and W. Xu, "Stability characteristics of medial meniscus tear in mild varus knee: a finite element analysis," *BMC Musculoskeletal Disorders*, vol. 26, no. 1, p. 897, 2025.

[28] Z. Zheng, Y. Liu, A. Zhang, H. Chen, Q. Wan, L. Zhong, X. Wang, Q. Han, and J. Wang, "Medial-lateral translational malalignment of the prosthesis on tibial stress distribution in total knee arthroplasty: A finite element analysis," *Frontiers in Bioengineering and Biotechnology*, vol. 11, p. 1119204, 2023.

[29] H. Razi, J. Predan, F. D. Fischer, O. Kolednik, and P. Fratzl, "Damage tolerance of lamellar bone," *Bone*, vol. 130, p. 115102, 2020.

[30] G. A. Orozco, P. Tanska, A. Gustafsson, R. K. Korhonen, and H. Isaksson, "Crack propagation in articular cartilage under cyclic loading using cohesive finite element modeling," *Journal of the Mechanical Behavior of Biomedical Materials*, vol. 131, p. 105227, 2022.

[31] A. Dorogoy, D. Rittel, K. Shemtov-Yona, and R. Korabi, "Modeling dental implant insertion," *Journal of the Mechanical Behavior of Biomedical Materials*, vol. 68, pp. 42–50, 2017.

[32] K. Singh *et al.*, "A comparative analysis of insertion of dental implants of v, square and trapezoidal screw designs," *Next Research*, vol. 2, p. 100462, 2025.

[33] Z. Trad, A. Barkaoui, and M. Chafra, "A three dimensional finite element analysis of mechanical stresses in the human knee joint: Problem of cartilage destruction," *Journal of Biomimetics, Biomaterials and Biomedical Engineering*, vol. 32, pp. 29–39, 2017.

[34] S. S. Chen, Y. H. Falcovitz, R. Schneiderman, A. Maroudas, and R. L. Sah, "Depth-dependent compressive properties of normal aged human femoral head articular cartilage: relationship to fixed charge density," *Osteoarthritis and Cartilage*, vol. 9, no. 6, pp. 561–569, 2001.

[35] T. Simkheada, G. A. Orozco, R. K. Korhonen, P. Tanska, and M. E. Mononen, "Comparison of constitutive models for meniscus and their effect on the knee joint biomechanics during gait," *Computer Methods in Biomechanics and Biomedical Engineering*, vol. 26, no. 16, pp. 2008–2021, 2023.

[36] X. Ma *et al.*, "Biomechanical impact of progressive meniscal extrusion on the knee joint: a finite element analysis," *Journal of Orthopaedic Surgery*, vol. 19, no. 1, p. 754, 2024.

[37] T. M. Guess and S. Razu, "Loading of the medial meniscus in the acl deficient knee: A multibody computational study," *Medical Engineering & Physics*, vol. 41, pp. 26–34, 2017.

[38] T. Guess, S. Razu, K. Kuroki, and J. Cook, "Function of the anterior intermeniscal ligament," *The Journal of Knee Surgery*, vol. 31, no. 1, pp. 068–074, 2018.

[39] Y. S. Lee, S. H. Oh, J. K. Seon, E. K. Song, and T. R. Yoon, "3d femoral neck anteversion measurements based on the posterior femoral plane in orthodoc® system," *Medical & Biological Engineering & Computing*, vol. 44, no. 10, pp. 895–906, 2006.

[40] G. McDaniel, K. L. Mitchell, C. Charles, and V. B. Kraus, "A comparison of five approaches to measurement of anatomic knee alignment from radiographs," *Osteoarthritis and Cartilage*, vol. 18, no. 2, pp. 273–277, 2010.

[41] S. J. Jang *et al.*, "Comparison of tibial alignment parameters based on clinically relevant anatomical landmarks: a deep learning radiological analysis," *Bone & Joint Open*, vol. 3, no. 10, pp. 767–776, 2022.

[42] A. H. Brănescu, I.-C. Lebădă, V. Mihuţ, N. Marjanovic, and M. Rackov, "Cad modelling of the human femur taking into account the structure of the bone," *MATEC Web of Conferences*, vol. 343, p. 04010, 2021.

[43] K. Daszkiewicz and P. Łuczkiewicz, "Biomechanics of medial meniscus tears in the context of pain: a finite element analysis," *Frontiers in Bioengineering and Biotechnology*, vol. 13, p. 1693500, 2026.

[44] E. Peña, B. Calvo, M. A. Martínez, D. Palanca, and M. Doblaré, "Finite element analysis of the effect of meniscal tears and meniscectomies on human knee biomechanics," *Clinical Biomechanics*, vol. 20, no. 5, pp. 498–507, 2005.

[45] C. Öhman *et al.*, "Compressive behaviour of child and adult cortical bone," *Bone*, vol. 49, no. 4, pp. 769–776, 2011.

[46] L. Rincón-Kohli and P. K. Zysset, "Multi-axial mechanical properties of human trabecular bone," *Biomechanics and Modeling in Mechanobiology*, vol. 8, no. 3, pp. 195–208, 2009.

[47] A. Ristaniemi, J. Tuppurainen, J. Jäntti, E. Nippolainen, I. O. Afara, M. E. Mononen, R. K. Korhonen, and J. T. Mäkelä, "Comparison of site-specific tensile, compressive, and friction properties of human tibiofemoral joint cartilage and their relationship to degeneration," *Journal of Biomechanics*, vol. 177, p. 112386, 2024.

[48] J. Schwer, A. Ignatius, and A. M. Seitz, "The biomechanical properties of human menisci: A systematic review," *Acta Biomaterialia*, vol. 175, pp. 1–26, 2024.

[49] D. Pan *et al.*, "Effects of proximal fibular osteotomy on stress changes in mild knee osteoarthritis with varus deformity: a finite element analysis," *Journal of Orthopaedic Surgery*, vol. 15, no. 1, p. 375, 2020.

[50] A. Haris and V. B. C. Tan, "Stress response envelopes of intact tibiofemoral joint and knee osteoarthritis," *Proceedings of the Institution of Mechanical Engineers, Part H: Journal of Engineering in Medicine*, vol. 234, no. 10, pp. 1151–1161, 2020.

[51] O. Kolednik, R. Schöngrundner, and F. Fischer, "A new view on j-integrals in elastic–plastic materials," *International Journal of Fracture*, no. 187, pp. 77–107, 2014.

[52] R. Upadhyaya, S. Sunil, R. Singh, and A. Tiwari, "Crack in presence of holes: Experimental measurements and configurational force analysis," *TAFM*, vol. 138, p. 104951, 2025.